Article

Structural insights into cytokine cleavage by inflammatory caspase-4

https://doi.org/10.1038/s41586-023-06751-9

Received: 17 May 2023

Accepted: 16 October 2023

Published online: 22 November 2023

Check for updates

Pascal Devant[1,5], Ying Dong[2,3,5], Julian Mintseris[4], Weiyi Ma[1], Steven P. Gygi[4], Hao Wu[2,3]✉ & Jonathan C. Kagan[1]✉

Inflammatory caspases are key enzymes in mammalian innate immunity that control the processing and release of interleukin-1 (IL-1)-family cytokines[1,2]. Despite the biological importance, the structural basis for inflammatory caspase-mediated cytokine processing has remained unclear. To date, catalytic cleavage of IL-1-family members, including pro-IL-1β and pro-IL-18, has been attributed primarily to caspase-1 activities within canonical inflammasomes[3]. Here we demonstrate that the lipopolysaccharide receptor caspase-4 from humans and other mammalian species (except rodents) can cleave pro-IL-18 with an efficiency similar to pro-IL-1β and pro-IL-18 cleavage by the prototypical IL-1-converting enzyme caspase-1. This ability of caspase-4 to cleave pro-IL-18, combined with its previously defined ability to cleave and activate the lytic pore-forming protein gasdermin D (GSDMD)[4,5], enables human cells to bypass the need for canonical inflammasomes and caspase-1 for IL-18 release. The structure of the caspase-4–pro-IL-18 complex determined using cryogenic electron microscopy reveals that pro-IL-18 interacts with caspase-4 through two distinct interfaces: a protease exosite and an interface at the caspase-4 active site involving residues in the pro-domain of pro-IL-18, including the tetrapeptide caspase-recognition sequence[6]. The mechanisms revealed for cytokine substrate capture and cleavage differ from those observed for the caspase substrate GSDMD[7,8]. These findings provide a structural framework for the discussion of caspase activities in health and disease.

Cytokines of the IL-1 family are central regulators of inflammation and immunity[1]. In contrast to most cytokines, several members of the IL-1 family, including IL-1β and IL-18, are synthesized as inactive cytoplasmic pro-proteins of which the N termini must be cleaved to achieve bioactivity[1]. After release into the extracellular space from living cells or by a lytic form of cell death known as pyroptosis[9–12], IL-1β and IL-18 can bind to inflammation-inducing receptors on neighbouring cells. Owing to the potent inflammatory activities of the IL-1 family and their importance in immunity, attention has focused on defining regulators of cleavage and release of these cytokines[3]. Much progress in this area has come from the study of pro-IL-1β, of which the principal mechanism of cleavage functions through the actions of canonical inflammasomes[13]. Inflammasomes are cytoplasmic supramolecular organizing centres[14], the assembly of which is seeded by proteins such as NLRP3[13]. These supramolecular organizing centres function as the subcellular site of caspase-1 activation, which was originally identified as interleukin-1-converting enzyme (ICE)[15]. Inflammasome-associated caspase-1 cleaves pro-IL-1β and the latent pore-forming protein GSDMD to mediate the release of IL-1β[4,5,10,11,15]. Related caspases, such as human caspase-4 and -5 and mouse caspase-11, are not recruited into inflammasomes and cannot cleave IL-1β efficiently[16–19]. Rather, these latter enzymes mediate IL-1β cleavage indirectly, as they can act upstream of the NLRP3 inflammasome after binding to bacterial lipopolysaccharides (LPS) (known as non-canonical inflammasome activation)[20–23]. Caspase-4, but not caspase-5, has been implicated in the cleavage of the IL-1 family cytokine pro-IL-18, but the cleavage preference for this cytokine is undefined[17,24,25]. Despite these insights into IL-1 biology, fundamental gaps in our knowledge of this cytokine family remain. In particular, structural insights into how any caspase interacts with its cytokine substrate are lacking.

Here we report that pro-IL-18 is the preferred IL-1 family substrate of caspase-4, enabling canonical-inflammasome-independent cleavage and release of IL-18 from human myeloid cells. We also report a cryogenic electron microscopy (cryo-EM) structure of the caspase-4–pro-IL-18 complex, revealing molecular insights into substrate recognition, cleavage and release by this inflammatory caspase.

Caspase-4 is an IL-18-converting enzyme

We began our study by examining the ability of caspase-4 to cleave multiple IL-1-family pro-cytokines in a quantitative in vitro cleavage assay using purified components. The catalytic domain of caspase-4 was expressed in *Escherichia coli*, in which autoprocessing occurs to yield active caspases consisting of the large p20 and the small p10

[1]Division of Gastroenterology, Boston Children's Hospital and Harvard Medical School, Boston, MA, USA. [2]Department of Biological Chemistry and Molecular Pharmacology, Harvard Medical School, Boston, MA, USA. [3]Program in Cellular and Molecular Medicine, Boston Children's Hospital, Boston, MA, USA. [4]Department of Cell Biology, Harvard Medical School, Boston, MA, USA. [5]These authors contributed equally: Pascal Devant, Ying Dong. ✉e-mail: wu@crystal.harvard.edu; jonathan.kagan@childrens.harvard.edu

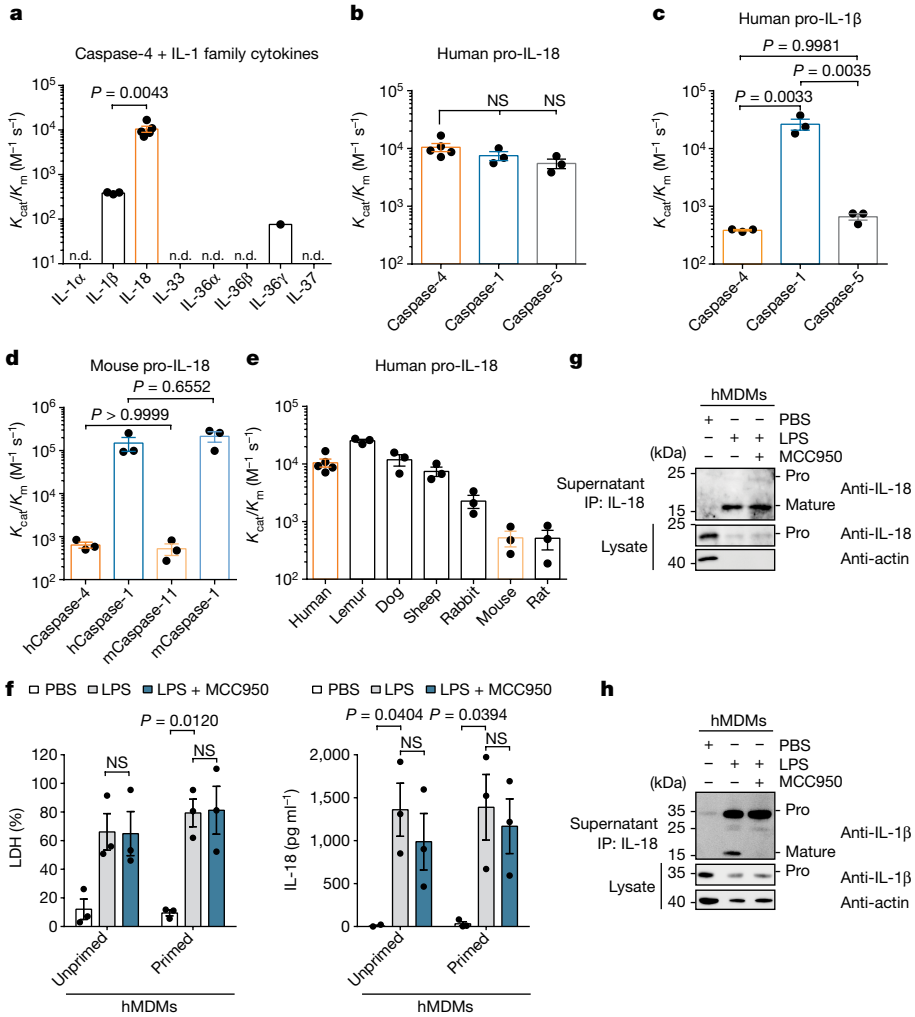

Fig. 1 | Human caspase-4 can efficiently cleave human pro-IL-18 but not other IL-1-family cytokines. a, In vitro cleavage of human IL-1-family cytokines by human caspase-4. n.d., cleavage not detected. **b**–**d**, In vitro cleavage of human (h) (**b**) or mouse (m) (**d**) pro-IL-18, or human pro-IL-1β (**c**) by the indicated caspases. **e**, In vitro cleavage of different mammalian pro-IL-18 homologues by species-matched caspase-4 homologues. For **a**–**e**, $n = 3$ biological replicates for all substrate–enzyme pairs, except for human caspase-4 + human pro-IL-18, for which $n = 4$. **f**–**h**, Primary hMDMs were primed with LPS, or left unprimed, and electroporated with LPS (or PBS), and LDH and IL-18 release into the cell culture supernatant was quantified after 2 h (**f**). $n = 3$ biological replicates with cells from different donors. IL-18 (**g**) or IL-1β (**h**) was immunoprecipitated from the cell culture supernatants of LPS-primed hMDMs and analysed using immunoblotting. Where indicated, NLRP3 was inhibited with 10 μM MCC950. Immunoblots are representative of three biological replicates. Each datapoint represents the result of one independent assay. For **a**–**f**, data are mean ± s.e.m. Statistical significance was determined using one-way analysis of variance (ANOVA) (**a**–**d**) or two-way ANOVA (**f**) with Tukey's multiple-comparison test; NS, not significant ($P > 0.05$). Gel source data are provided in Supplementary Fig. 1.

catalytic subunits (Extended Data Fig. 1a). Serially diluted caspase-4 was incubated with a fixed concentration of substrate and the kinetic parameters were derived by determining the enzyme concentration at which 50% of the substrate is consumed[26]. Most of the tested IL-1-family cytokines (pro-IL-1α, pro-IL-33, pro-IL-36α, pro-IL-36β and pro-IL-37) were not cleaved by caspase-4 (Fig. 1a and Extended Data Fig. 1b–i). Of the cytokines that were cleaved, pro-IL-18 was cleaved with 30-fold to greater than 100-fold higher catalytic efficiency than the others (pro-IL-1β and pro-IL-36γ) (Fig.1a and Extended Data Fig. 1b,c,h). Notably, caspase-4 was as efficient at cleaving pro-IL-18 as the ICE caspase-1, consistent with previous reports[17] (Fig. 1b and Extended Data Fig. 1j). Contrary to the published literature[17], pro-IL-18 was also cleaved efficiently by human caspase-5, an orthologue of caspase-4 (Fig. 1b and Extended Data Fig. 1k). Pro-IL-1β, which is cleaved with high efficiency by caspase-1, was poorly cleaved by caspase-4 or caspase-5 (Fig. 1c and Extended Data Fig. 1d,l,m). We noted that human caspase-4 and its mouse homologue caspase-11 possessed low activity towards mouse pro-IL-18, whereas human and mouse caspase-1 cleaved mouse pro-IL-18 efficiently (Fig. 1d and Extended Data Fig. 1n–q). We extended this analysis to caspase-4 homologues from other mammalian species. Analogous enzymes from dog, lemur, rabbit and sheep cleaved species-matched pro-IL-18 homologues with an efficiency comparable to human caspase-4 cleavage of human pro-IL18 (Fig. 1e and Extended Data Fig. 1r–u). By contrast, the caspase-4 homologues from mice and rats (known as caspase-11) displayed a weak ability to cleave pro-IL-18 (Fig. 1e and Extended Data Fig. 1p,v). Mouse caspase-11 also cleaved human pro-IL-18 with a low efficiency (Extended Data Fig. 1w,x). These results suggest that caspase-4 from multiple species, except rodents, represents an IL-18-converting enzyme.

Caspase-4 links LPS detection to IL-18 release

The ability of human caspase-4 to bind to LPS and cleave pro-IL-18 and GSDMD should, in principle, bypass the need for the NLRP3 inflammasome to mediate IL-18 release from cells. Conversely, the inability of mouse caspase-11 to cleave pro-IL-18 should result in a dependence

on inflammasome-associated caspase-1 to cleave and release IL-18 from cells. In human epithelial cells (such as HeLa cells), which lack NLRP3, these predictions are supported by previous reports, in which bacteria induced IL-18 release through a caspase-4-dependent but caspase-1-independent process[24,25,27–29]. This concept has yet to be tested in human cells competent for NLRP3 signalling, such as myeloid cells. We tested these predictions by delivering LPS into the cytosol of THP1 monocytes, in which caspase-4 and pro-IL-18 are constitutively expressed[20,30]. We also examined THP1 monocytes in which NLRP3 signalling was disrupted by genetic deficiency or through the use of the small-molecule inhibitor MCC950[31]. Electroporation of wild-type (WT) THP1 cells with LPS induced pyroptosis, as indicated by release of the cytosolic enzyme lactate dehydrogenase (LDH) into the extracellular space, whereas cells that were electroporated with PBS remained alive (Extended Data Fig. 2a). Pyroptosis was independent of NLRP3, as neither treatment with MCC950 nor knockout (KO) of *NLRP3* prevented LDH release. NLRP3 was not required for LPS-induced release of IL-18 into the cell culture supernatant as shown by enzyme-linked immunosorbent assay (ELISA) (Extended Data Fig. 2b). Importantly, we confirmed that the IL-18 ELISA preferentially detects cleaved IL-18, as compared to pro-IL-18 (Extended Data Fig. 2c). We also confirmed by immunoblotting that cleavage of pro-IL-18 still occurred when NLRP3 function was blocked (Extended Data Fig. 2d,e). By contrast, LPS-induced cleavage of pro-IL-1β was prevented in NLRP3-deficient or MCC950-treated THP1 cells after LPS electroporation (Extended Data Fig. 2f,g). Similar observations were made in primary human monocyte-derived macrophages (hMDMs), in which LPS-induced processing and release of IL-18, but not IL-1β, was unaffected by NLRP3 inhibition with MCC950 (Fig. 1f–h).

To test the caspase-dependency of IL-18 release from human cells, we generated clonal THP1 cell lines deficient for genes encoding caspase-1 or caspase-4 using CRISPR–Cas9 (Extended Data Fig. 2h). Pyroptosis and IL-18 release in response to LPS electroporation was reduced in caspase-4-deficient cells, but not in caspase-1-deficient cells, as compared to cells that were transfected with a non-targeting single guide RNA (sgRNA) (Extended Data Fig. 2i). By contrast, cleavage and release of IL-1β was diminished in both caspase-1-deficient and caspase-4-deficient cells (Extended Data Fig. 2j). We were unable to detect the caspase-5 protein in any of these cell lines (Extended Data Fig. 2k). However, consistent with its ability to efficiently cleave pro-IL-18 in vitro (Fig. 1b), expression of caspase-5 in caspase-4-deficient THP1 cells enabled cytosolic LPS-induced IL-18 release, which was insensitive to MCC950 (Extended Data Fig. 2l,m). Finally, pyroptosis and IL-18 release from THP-1 macrophages was NLRP3 independent after infection with a flagellin-deficient strain of *Salmonella enterica* serovar Typhimurium[32] (Extended Data Fig. 2n). No IL-18 release was observed when caspase-4-deficient THP1 macrophages were infected with these bacteria (Extended Data Fig. 2n). Collectively, these data demonstrate that caspase-4 and caspase-5 cleave pro-IL-18 in vitro and in cells, which enables these enzymes to intrinsically link LPS detection to IL-18 cleavage and release. Moreover, the requirement for NLRP3 and caspase-1 for IL-1β release under all conditions examined suggests that the weak in vitro cleavage activities of pro-IL-1β by caspase-4 are negligible in the context of cells.

In contrast to our findings in human cells, different observations were made in mouse immortalized bone-marrow-derived macrophages (iBMDMs). Consistent with previous reports[23] and the poor cleavage of pro-IL-18 by caspase-11 in vitro (Fig. 1d), NLRP3 was required for IL-18 and IL-1β cleavage and release after LPS electroporation of iBMDMs (Extended Data Fig. 3a–e). To determine whether we could convert human cells into cells that require NLRP3 for IL-18 release, akin to mouse cells, we expressed caspase-11 in caspase-4-deficient THP1 cells (Extended Data Fig. 3f). We found that THP1 macrophages expressing caspase-11 underwent pyroptosis and released IL-18 in response to LPS electroporation, but IL-18 release from caspase-11-expressing THP1 cells was reduced when NLRP3 activation was blocked by MCC950 (Extended Data Fig. 3g). These results reveal the ability of human caspase-4, but not mouse caspase-11, to function as a sensor and effector that mediates cleavage and release of IL-18, independent of canonical inflammasomes. This one-protein signalling pathway—whereby caspase-4 links LPS detection to pro-IL-18 cleavage and release through GSDMD—is similar to that which we have described in several species of carnivora[16]. These animals, including felines, bears and seals, encode a caspase known as caspase-1/4, which intrinsically links LPS detection to IL-1β cleavage and release from cells[16].

Structure of the caspase-4–pro-IL-18 complex

To define the interaction between caspase-4 and pro-IL-18 at the molecular level, we determined the cryo-EM structure of caspase-4 in complex with pro-IL-18. We assembled a complex consisting of recombinant human caspase-4 (large p20 subunit carrying an inactivating C258A mutation + small p10 subunit) and human pro-IL-18 (Fig. 2a and Extended Data Fig. 4). Before making EM grids, the complex was stabilized with the chemical cross-linker BS3 and repurified by size-exclusion chromatography (SEC). The size and composition of the complex was validated by SDS–PAGE and blue native PAGE (Extended Data Fig. 4). Cryo-EM data were collected in 5,934 raw videos, and two-dimensional (2D) classification revealed the existence of different orientations of the complex and molecular details (Fig. 2b). After multiple rounds of 2D and 3D classification followed by refinement with imposed twofold symmetry of a best class consisting of 229,147 particles, we obtained a cryo-EM map of the caspase-4–pro-IL-18 complex at a resolution of 3.2 Å (Extended Data Fig. 5 and Extended Data Table 1). Overall, the regions of the density comprising caspase-4 and the part of pro-IL-18 proximal to caspase-4 are best-defined, whereas the distal ends of pro-IL-18 are less ordered (Fig. 2c). We applied focused refinement on IL-18, which improved the overall resolution in this region of the map to 3.1 Å resolution (Fig. 2d), but the resulting map had similar quality at the caspase-4–pro-IL-18 interface to the complete map. The lower resolution in the distal part of the map is probably due to the dynamic nature of the complex shown by 3D variability analysis (Fig. 2c,d, Extended Data Fig. 5b and Supplementary Video 1).

The cryo-EM structure of the caspase-4–pro-IL-18 complex has a symmetric wrapped-sweet-shaped architecture, in which two pro-IL-18 molecules are bound to the caspase-4 dimer-of-heterodimers (heterotetramer) consisting of two copies of p20/p10 (Fig. 3a). The density fitting was initiated with the crystal structure of caspase-4[7] and mature IL-18[33]. While the caspase-4 structure matched the density well, the IL-18 structure exhibited substantial differences from the density of pro-IL-18. We traced these differences to construct an atomic model of pro-IL-18. The final model includes the caspase-4 heterotetramer and pro-IL-18 with the near complete pro-domain (residues 6–36). Two regions in pro-IL-18 (residues 1–5, 53–80) are absent, probably due to disorder. The model was independently validated by cross-linking mass spectrometry (MS), with all intermolecular cross-links consistent with the structure (Extended Data Fig. 6a,b).

The cryo-EM structure of caspase-4–pro-IL-18 revealed two binding interfaces between caspase-4 and pro-IL-18, defined as the active site interface and the exosite interface (Fig. 3b,c). Pro-IL-18 buries extensive surface areas of approximately 800 $Å^2$ and 650 $Å^2$ at the active site and exosite, respectively[34]. Caspase substrates are often defined by the tetrapeptide sequences, that is, the four amino acid residues directly upstream of the scissile peptide bond (33-LESD-36 in pro-IL-18)[6]. In our structure, ordered density exists for the region before and after Asp36 in pro-IL-18 (β4′ and the adjacent linkers), among which residues Glu28–Phe38 interact with caspase-4 to form the active-site interface (Fig. 3d). The active-site interface is dominated by electrostatic interactions, which position this tetrapeptide in the substrate-binding cleft of

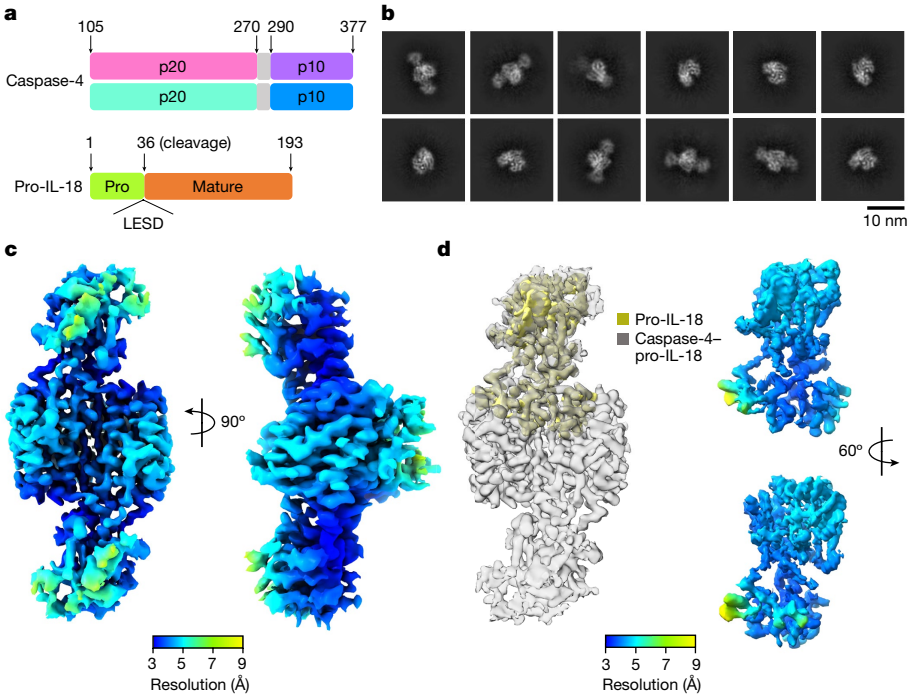

Fig. 2 | Overview of the caspase-4–pro-IL-18 complex. a, The domain organization of caspase-4 and pro-IL-18. The caspase-4 large subunits (p20) are shown in cyan or pink; the small subunits (p10) are shown in purple or blue; the linker regions between p20 and p10 are shown in grey, which is absent in the model; and the pro-domain and mature domain of pro-IL-18 are shown in green and orange, respectively. **b**, Representative 2D classes of the caspase-4–pro-IL-18 complex. Scale bar, 10 nm. **c**, The complete map of the caspase-4–pro-IL-18 complex at an overall resolution of 3.2 Å (contour level, 3.0σ), coloured by local resolution. **d**, Focus-refined map of pro-IL-18 (yellow) at an overall resolution of 3.1 Å (contour level, 3.4σ), superimposed with the complete map (grey) (left) or coloured by local resolution in two views (right).

caspase-4. We observed paired charge–charge interactions between Glu28 and Lys293, Asp30 and Lys356, and Glu34 and Arg314 in pro-IL-18 and caspase-4, respectively. The cleavage-site residue Asp36 interacts with Arg152, Gln256 and Arg314 of caspase-4. The alanine mutation on the catalytic Cys258 residue of caspase-4 enables the binding of the pro-IL-18 substrate at the active site without being cleaved. However, in active caspase-4, the scissile peptide bond at the C terminus of Asp36 and the catalytic centre of caspase-4 (Cys258) would be in proximity, enabling cleavage (Extended Data Fig. 6c).

In contrast to the electrostatic active-site interface, the exosite interface is defined by hydrophobic and electrostatic interactions (Fig. 3e). Trp267 of caspase-4 is inserted into a hydrophobic pocket formed by Val47 and Ile48 of pro-IL-18 (Fig. 3e). The interaction is enhanced by the interactions of Glu192 and Asp193 of pro-IL-18 with Arg269 in the p10 subunit of caspase-4 (Fig. 3e). Similar interactions have been observed at the exosite of inflammatory caspase–GSDMD complexes, suggesting a common mechanism for inflammatory caspases to capture different substrates to enhance their cleavage activity[7,8]. Notably, due to the limited resolution of the cryo-EM density in this region, we suspect that additional conformations may exist in which Arg49 of pro-IL-18 interacts with Trp267 through cation–π interactions.

The conformational difference between pro-IL-18 in a complex with caspase-4 and mature IL-18 can be visualized as the insertion of the pro-domain as β-strands into the β-trefoil fold in the mature domain (Extended Data Fig. 6d,e). The N-terminal β2 and β3 strands of the mature domain partly unfold and change conformation in the bound conformation of pro-IL-18 to form the hydrophobic pocket at the exosite interface. These observations indicate that newly cleaved IL-18 undergoes conformational changes to arrive at the structure of the mature IL-18. Cross-linking MS data of pro-IL-18 alone and in the caspase-4–pro-IL-18 complex suggest conformational differences in pro-IL-18 before and after caspase-4 interaction (Extended Data Fig. 6f,g). AlphaFold[35] predicted a structure of pro-IL-18, in which the pro-domain is localized at the opposite end to where the pro-domain is localized in our caspase-bound structure. Nevertheless, the predicted pro-domain contains certain β-strand elements that are consistent with the caspase-4–pro-IL-18 complex (Extended Data Fig. 6h). Thus, it appears that pro-IL-18 is conformationally adaptable and may have at least three conformations: the apo state and states after caspase binding and after cleavage.

Active-site interactions define cleavage

After engagement of a hydrophobic exosite, inflammatory caspases cleave GSDMD in a tetrapeptide-independent manner[7]. This is not the case for pro-IL-18, as mutating the tetrapeptide sequence in pro-IL-18 from LESD to AAAD decreased cleavage by caspase-4 (Fig. 4a and Extended Data Fig. 7a). Thus, the tetrapeptide of pro-IL-18 promotes cleavage by caspase-4. However, the tetrapeptide is not sufficient for efficient cleavage by caspase-4, as we found that mouse pro-IL-18, which shares the same tetrapeptide sequence with human pro-IL-18, is poorly cleaved (Fig. 1d and Extended Data Fig. 7b). Consistent with this idea, a chimeric pro-IL-18 variant consisting of the pro-domain of mouse pro-IL-18 and the mature domain of human IL-18 was cleaved less efficiently by caspase-4 compared with WT human pro-IL-18 and did not form a stable complex with caspase-4 (Fig. 4a,b and Extended Data Fig. 7c). These results indicate that the higher catalytic efficiency of caspase-4 for human versus mouse pro-IL-18 can at least partially be explained by amino acid residues in the pro-domain of human pro-IL-18. To test this idea, we determined the impact of amino acid swaps between human and mouse pro-IL-18 on cleavage

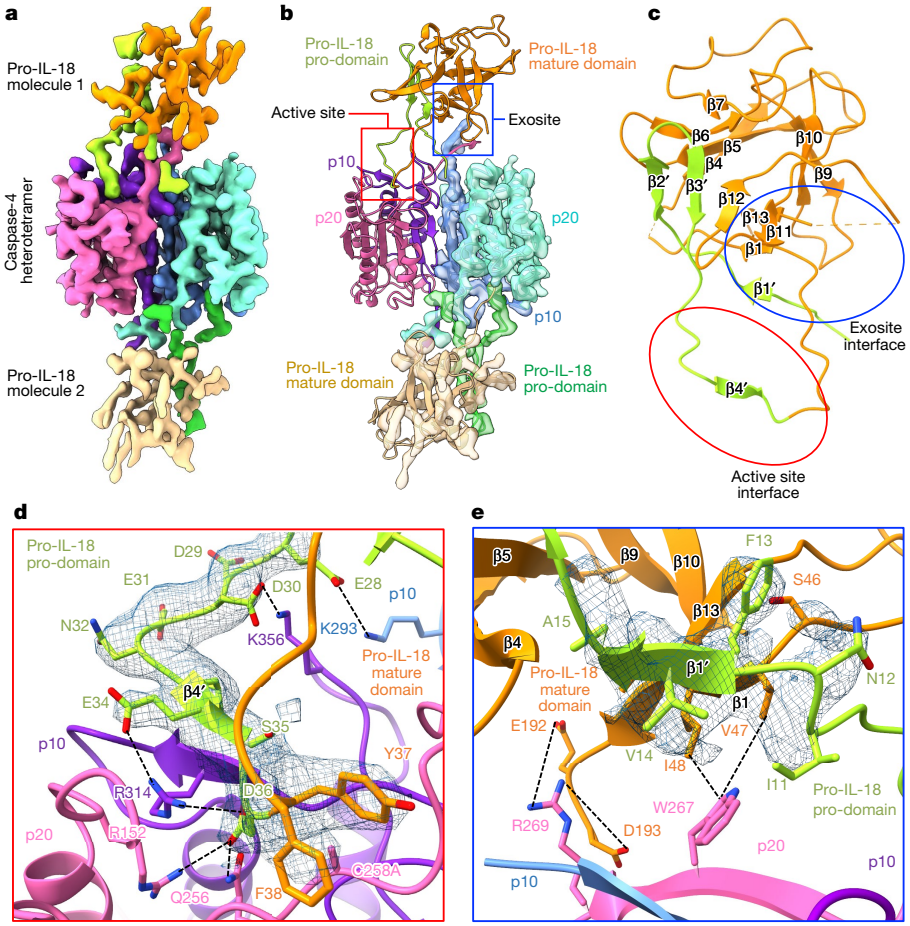

Fig. 3 | Cryo-EM map and model of the caspase-4–pro-IL-18 complex. **a**, Cryo-EM map of the caspase-4–pro-IL-18 complex coloured by domains (contour level, 3.0σ). **b**, The caspase-4–pro-IL-18 complex model shown in the colour code as in **a**, alone for one half, and superimposed with the cryo-EM map for the other half. The active site and exosite are indicated by red and blue squares, respectively. **c**, The pro-IL-18 structure with secondary structures labelled; the two interfaces are indicated by red and blue ovals. **d**, Detailed interaction interface at the active site. **e**, Detailed interaction interface at the exosite. The cryo-EM density for the relevant pro-IL-18 region is shown as a blue mesh in **d** and **e**.

by caspase-4. Our cryo-EM structure suggests that Lys356 in caspase-4 forms electrostatic interactions with Asp30 in pro-IL-18. We found that swapping a stretch of amino acids surrounding this site in mouse pro-IL-18 to the respective human-specific residues (ENGD28DDEN) led to an increase in the catalytic efficiency of caspase-4 (Fig. 4c). By combining this mutation with additional human-specific mutations (N36Y and H41E), we generated a 'humanized' mouse pro-IL-18 triple mutant that is cleaved by caspase-4 almost as efficiently as human pro-IL-18 in vitro (Fig. 4c and Extended Data Fig. 7d–h). We detected higher amounts of IL-18 in the supernatants of IL-18-deficient THP1 cells expressing humanized mouse pro-IL-18 compared with in the supernatants of THP1 cells expressing WT mouse pro-IL-18 after LPS electroporation in the presence of MCC950 (Fig. 4d,e). These data indicate that residues in the pro-domain, including but not limited to the tetrapeptide, promote binding and cleavage of pro-IL-18 by caspase-4.

We found that caspase-4 is unable to bind to mature IL-18, which lacks the pro-domain, as assessed by analytical SEC or isothermal titration calorimetry (ITC) (Fig. 4f and Extended Data Fig. 7i). Similarly, a truncated version of pro-IL-18, which lacks the first 24 amino acid residues of the pro-domain (named ΔN24), does not bind to caspase-4 and is cleaved less efficiently by caspase-4 (Fig. 4g and Extended Data Fig. 7j,k). Removal of the pro-domain of pro-IL-18 after cleavage may therefore facilitate the release of the bioactive cytokine from the enzyme.

Exosite mutations abolish IL-18 cleavage

Introduction of charge-reversing mutations in either of the interaction surfaces (K356D or R269D) or mutation of the hydrophobic residue at the core of the exosite to a polar residue (W267N) disrupted caspase-4 binding to pro-IL-18 in vitro (Fig. 5a and Extended Data Fig. 8a,b). As a result, in vitro cleavage of pro-IL-18 by caspase-4 variants carrying these mutations was reduced, with the W267N mutation having the greatest effect (Fig. 5b and Extended Data Fig. 8c–e). These mutations in caspase-4 did not interfere with intrinsic enzymatic activities, as the caspase-4 mutants retained the ability to cleave the chromogenic peptide substrate Ac-WEHD-pNA (Fig. 5c). Caspase-4(W267N) showed a small reduction in Ac-WEHD-pNA processing (as described previously[7]), but this effect is unlikely to explain the greater than 100-fold reduction in its ability to cleave pro-IL-18 (Fig. 5b). Reciprocal mutations in pro-IL-18 yielded symmetrical results to the mutagenesis of caspase-4. Perturbing the hydrophobic pocket or charge–charge interactions at the exosite interface by the introduction of V47N/I48N or E192K/D193K mutations decreased the binding of pro-IL-18 to caspase-4 (Fig. 5d and Extended Data Fig. 8f,g). Consequently, in vitro cleavage of these pro-IL-18 mutants by caspase-4 was decreased (Fig. 5e and Extended Data Fig. 8h–k).

To correlate these in vitro results with activities in cells, we reconstituted caspase-4-deficient THP1 cells with WT caspase-4 or caspase-4 mutants deficient in pro-IL-18 interaction (C258A, K356D, R269D and

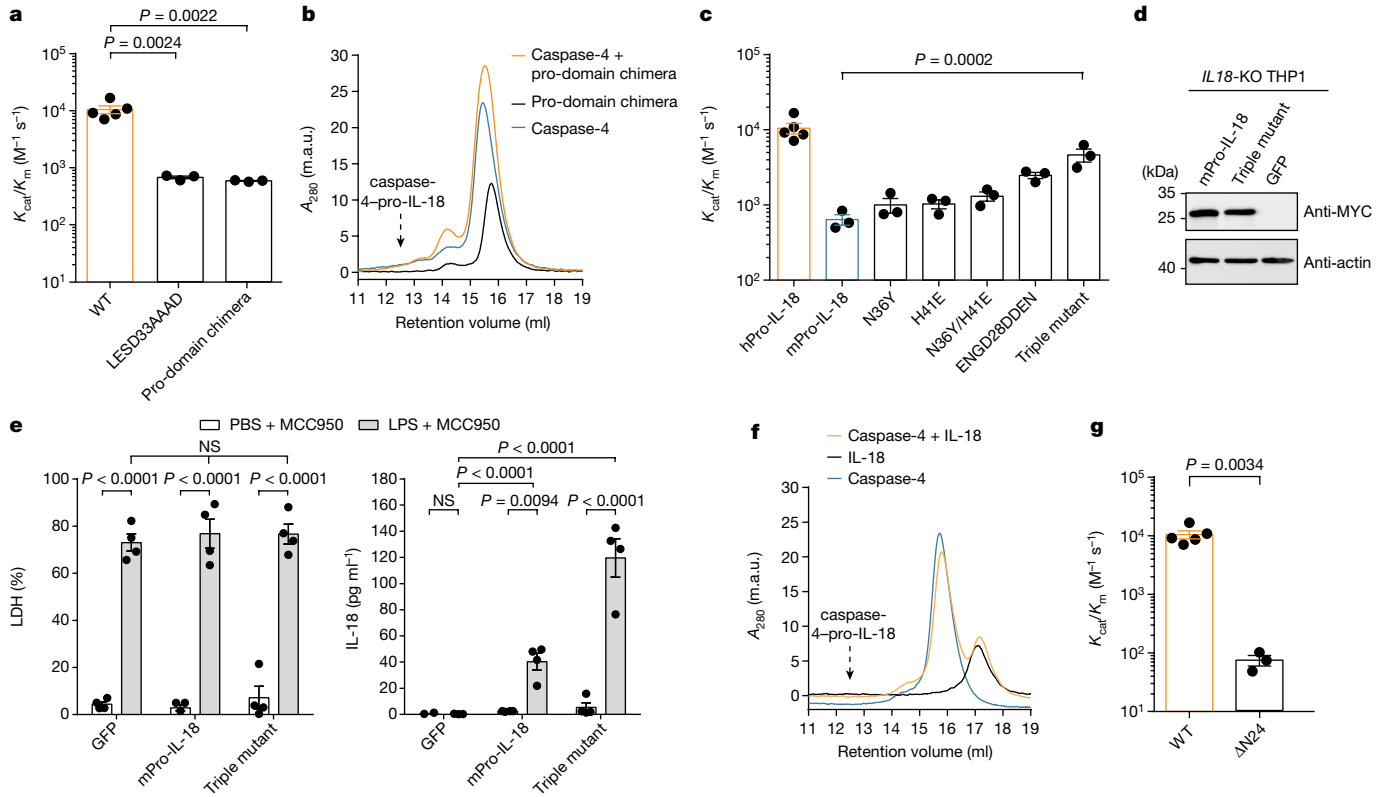

Fig. 4 | Electrostatic interactions between the pro-IL-18 pro-domain and caspase-4 promote cytokine processing. a, In vitro cleavage of human pro-IL-18 mutants by human caspase-4. The pro-domain chimera consists of the mouse pro-domain fused to the human mature domain. **b**, Analytical SEC showing no interaction between caspase-4 and the pro-domain chimera. The retention volume of the caspase-4–pro-IL-18 complex is marked. A_{280}, absorbance at 280 nm; m.a.u., milli-arbitrary units. **c**, In vitro cleavage of mouse pro-IL-18 variants by human caspase-4. The triple mutant combines all human-specific mutations (N36Y, H41E, ENGD28DDEN). **d**, Expression of MYC-tagged mouse pro-IL-18 variants in IL-18-deficient THP1 cells. **e**, IL-18-deficient THP1 macrophages expressing mouse pro-IL-18 variants were primed with LPS and electroporated with LPS (or PBS) in the presence of MCC950, and LDH and IL-18 release into the cell culture supernatant was quantified after 2 h. **f**, Analytical SEC analysis showing no interaction between mature IL-18 and caspase-4. **g**, In vitro cleavage of human pro-IL-18(ΔN24), which lacks the first 24 amino acids, by human caspase-4. SEC profiles and immunoblots are representative of three biological replicates. For **a**, **c** and **g**, $n = 3$ biological replicates for all substrate–enzyme pairs, except for WT caspase-4 + WT pro-IL-18, for which $n = 4$. For **e**, $n = 3$ biological replicates. Each datapoint represents the result of one independent assay. For **a**, **c**, **e** and **f**, data are mean ± s.e.m. Statistical significance was determined using unpaired two-sided Student's *t*-tests (**g**), one-way ANOVA (**a** and **c**) or two-way ANOVA (**e**) with Tukey's multiple-comparison test. Gel source data are provided in Supplementary Fig. 1.

W267N) (Extended Data Fig. 9a). These cells were electroporated with LPS in the presence of MCC950 to assess caspase-4-dependent pyroptosis and IL-18 release. Cells expressing WT caspase-4 underwent pyroptosis and released IL-18 in response to LPS electroporation, whereas cells expressing the catalytically inactive caspase-4(C258A) did not (Fig. 5f,g). Cytosolic LPS-induced LDH and IL-18 release from cells expressing caspase-4 carrying W267N, R269D or K356D mutations was reduced compared with release from cells expressing WT caspase-4 (Fig. 5f,g). This finding can be explained by the role of the same interfaces for GSDMD cleavage[7,8], which we confirmed experimentally in vitro and in cells (Extended Data Fig. 9b–g). To assess pro-IL-18 cleavage independently of GSDMD activities, we took advantage of the fact that our IL-18 ELISA is specific for cleaved IL-18 (Extended Data Fig. 3c). We assessed IL-18 abundance in combined cell lysates and supernatants by performing in-well lysis of cells, followed by ELISA and immunoblotting. These assays revealed that caspase-4(W267N) or caspase-4(K356D) mutants are as defective as the catalytic-site mutant caspase-4(C258A) in IL-18 generation (Fig. 5g and Extended Data Fig. 9h). Caspase-4(R269D) displayed the least severe defect in IL-18 generation after LPS electroporation (Fig. 5g and Extended Data Fig. 9h). We also reconstituted IL-18-deficient THP1 cells with WT pro-IL-18 or pro-IL-18 variants carrying mutations in the exosite or active site interfaces (E192K/D193K, V47N/I48N, DDEN29ENGD, LESD33AAAD) (Extended Data Fig. 9i). After LPS electroporation in the presence of MCC950, cells expressing all pro-IL-18 variants underwent pyroptosis to similar extent (Extended Data Fig. 9j). By contrast, we detected reduced levels of IL-18 in the supernatants of cells expressing pro-IL-18(E192K/D193K), pro-IL-18(DDEN29ENGD) or pro-IL-18(LESD33AAAD) compared with cells expressing WT pro-IL-18 (Fig. 5h). We excluded cells expressing pro-IL-18(V47N/I48N) from this analysis, as this mutant displayed severely reduced reactivity with the ELISA reagent (Extended Data Fig. 9k). However, we confirmed reduced levels of LPS-induced cleavage of all of the tested mutant proteins (including pro-IL-18(V47N/I48N)) compared with WT pro-IL-18 by immunoblotting (Fig. 5i). These collective data indicate that hydrophobic and charge–charge interactions determine the ability of caspase-4 to operate as an IL-18-converting enzyme.

Structure-based engineering of caspase-11

Finally, we determined whether our structural insights may explain the differential pro-IL-18 cleavage abilities of human caspase-4 and mouse caspase-11. We fitted a crystal structure of caspase-11[7] into our caspase-4–pro-IL-18 map to generate a model of a hypothetical caspase-11–pro-IL-18 complex (Fig. 6a). In this complex, critical exosite residues Trp263 and Arg265 (corresponding to Trp267 and Arg269 in caspase-4) fit into the hydrophobic pocket in pro-IL-18, similar

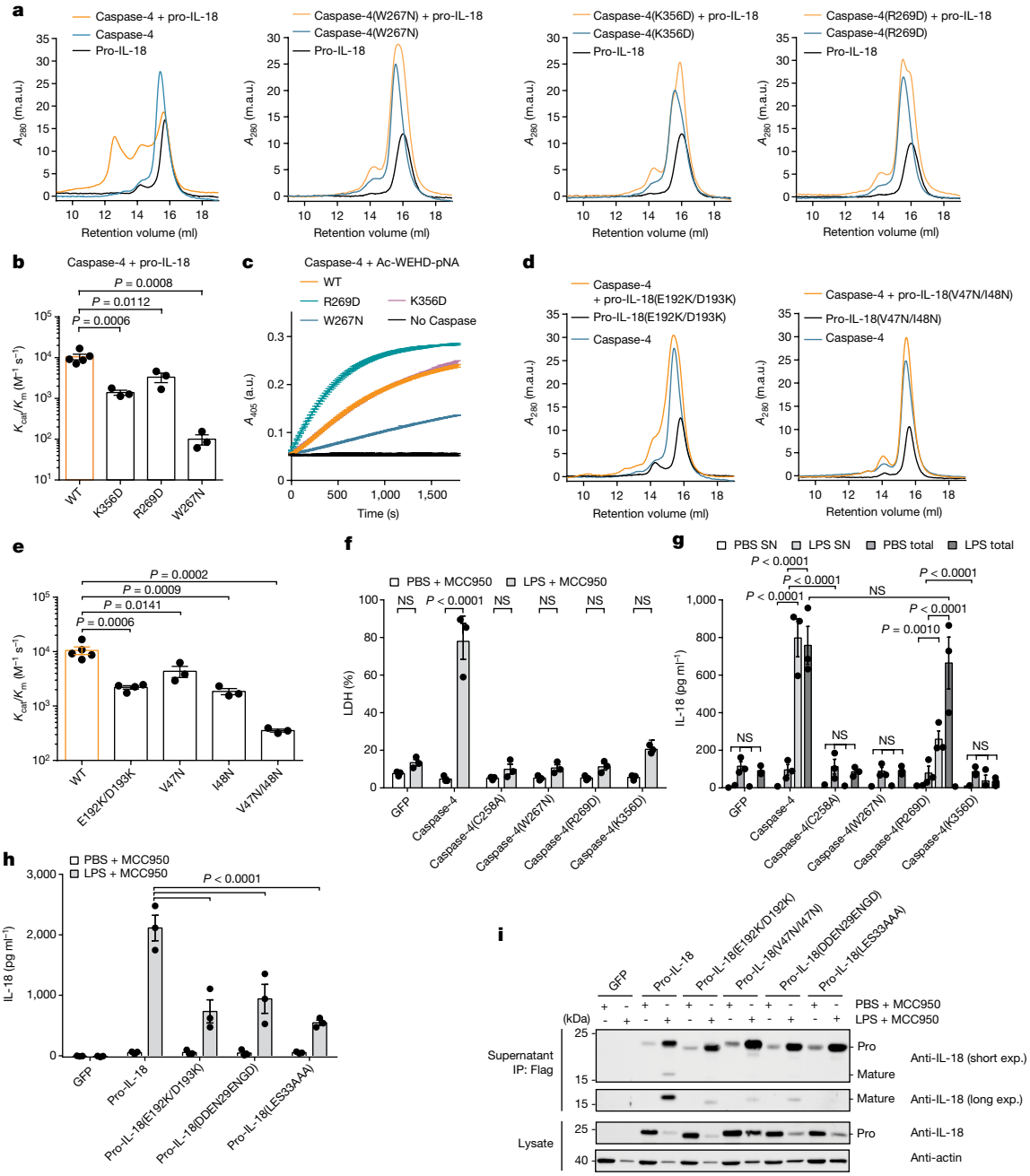

Fig. 5 | A hydrophobic exosite is required for recognition and cleavage of pro-IL-18 by caspase-4. a, Analytical SEC analysis of complex formation between pro-IL-18 (produced in insect cells) and the indicated caspase-4-p20/p10 mutants. **b**, In vitro cleavage of human pro-IL-18 by caspase-4 mutants. **c**, Kinetic analysis of the cleavage of the chromogenic peptide substrate Ac-WEHD-pNA by caspase-4 mutants. Data are mean ± s.d. of two technical replicates, representative of three biological replicates. a.u., arbitrary units. **d**, Analytical SEC analysis of complex formation between caspase-4-p20/p10 and the indicated pro-IL-18 mutants. Pro-IL-18 mutants were produced in *E. coli*. **e**, In vitro cleavage of human pro-IL-18 mutants by human caspase-4. **f**,**g**, Caspase-4-deficient THP1 macrophages expressing caspase-4 variants were primed with LPS and electroporated with LPS (or PBS) in the presence of MCC950, and LDH release was quantified after 2 h (**f**), and IL-18 levels in the supernatants (sup.) or total IL-18 levels (combined supernatants + cell lysates) were quantified using ELISA (**g**). **h**,**i**, IL-18-deficient THP1 macrophages expressing pro-IL-18 variants were primed with LPS and electroporated with LPS (or PBS) in the presence of MCC950 and the IL-18 levels in the supernatants were quantified after 2 h (**h**). IL-18 was immunoprecipitated from the supernatants using anti-Flag antibodies and analysed using immunoblotting (**i**). Immunoblots and SEC profiles are representative of three biological replicates. For **b** and **e**, $n = 3$ biological replicates for all substrate–enzyme pairs, except for WT caspase-4 + WT pro-IL-18 and pro-IL-18(E192K/D193K), for which $n = 4$. For **f**–**h**, $n = 3$ biological replicates. Each datapoint represents the result of one independent assay. For **b** and **e**–**h**, data are mean ± s.e.m. Statistical significance was determined using one-way ANOVA (**b** and **e**) or two-way ANOVA (**f**, **g** and **h**) with Tukey's multiple-comparison test. Gel source data are provided in Supplementary Fig. 1.

to what we observed in the caspase-4–pro-IL-18 complex (Fig. 6b). However, several critical interactions in the active-site interface are absent in the caspase-11–pro-IL-18 complex (Fig. 6b). Specifically, we found that the regions surrounding Lys356 and Lys293 in caspase-4, which interact with Glu28 and Asp30 in pro-IL-18, are not conserved in caspase-11 (Extended Data Fig. 10a). Instead, caspase-11 displays

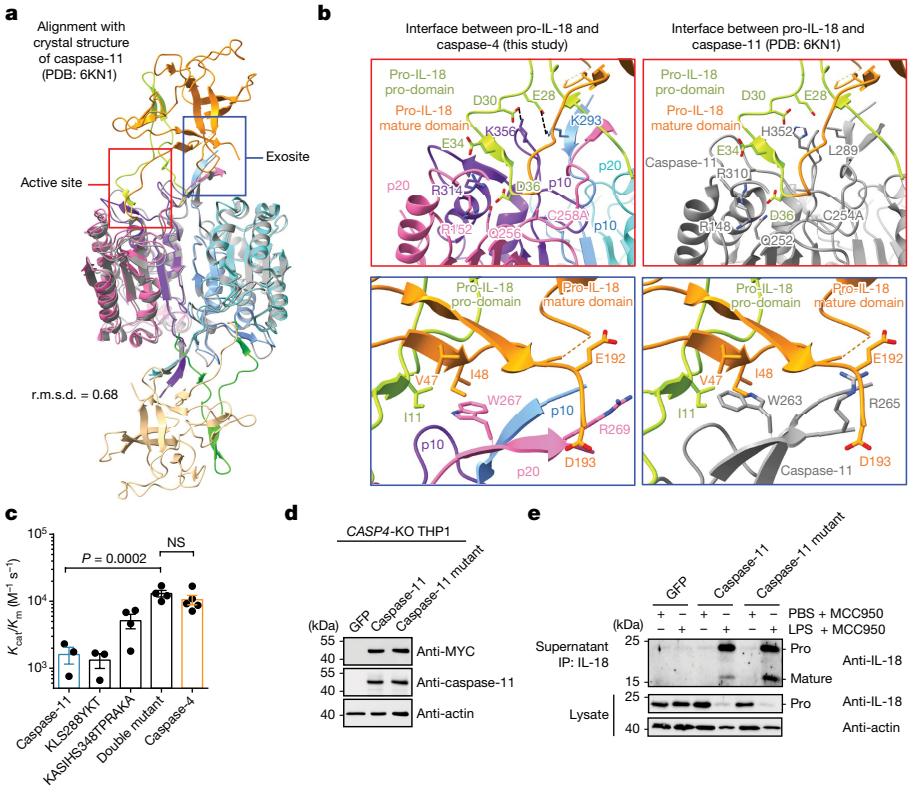

Fig. 6 | Engineering of caspase-11 into an efficient IL-18-converting enzyme. **a**, The structural model of a caspase-11–pro-IL-18 complex aligned with the experimentally determined caspase-4–pro-IL-18 cryo-EM structure. r.m.s.d., root mean squared deviation. **b**, Active-site and exosite interfaces in the caspase-11–pro-IL-18 model compared with in the caspase-4–pro-IL-18 structure. **c**, In vitro cleavage of human pro-IL-18 by caspase-11 mutants. $n = 4$ (caspase-4 and caspase-11(KASIHS348TPRAKA)) and $n = 3$ (all other proteins) biological replicates. **d**, Expression of caspase-11 variants in caspase-4-deficient THP1 cells. **e**, Caspase-4-deficient THP1 macrophages expressing caspase-11 variants were primed with LPS and electroporated with LPS (or PBS) in the presence of MCC950. After 2 h, IL-18 was immunoprecipitated from the cell culture supernatants and analysed using immunoblotting. The caspase-11 mutant in **d**,**e** combines KASIHS348TPRAKA and KLS288YKT mutations. Immunoblots are representative of two (**d**) or three (**e**) biological replicates. Each datapoint represents the result of one independent assay. For **c**, data are mean ± s.e.m. of at least three biological replicates. Statistical significance was determined using one-way ANOVA with Tukey's multiple-comparison test. Gel source data are provided in Supplementary Fig. 1.

non-charged residues (His352 and Leu289) at these sites. Introducing caspase-4-specific mutations at these sites in caspase-11 increased its ability to cleave pro-IL-18 in vitro to a level similar to caspase-4 (Fig. 6c and Extended Data Fig. 10b–d). We expressed this caspase-11 double mutant in caspase-4-deficient THP1 cells (Fig. 6d). When stimulated with cytosolic LPS in the presence of MCC950, we detected more mature IL-18 in the supernatants of cells expressing the caspase-11 double mutant compared with cells expressing WT caspase-11 (Fig. 6e). These data demonstrate that the differential efficiencies of pro-IL-18 cleavage between caspase-11 and caspase-4 can be explained by residues in the active-site interface.

Discussion

On the basis of the data presented, we propose a model for cytokine substrate capture, cleavage and release by caspase-4. Pro-IL-18 uses its pro-domain to interact with both neighbouring p10 subunits within the caspase-4 heterotetramer, which may stimulate dimerization of caspase-4 to promote its catalytic activity. We propose that pro-IL-18 binding and cleavage by caspase-4 relies on a unique bivalent mode of recognition. In addition to binding of a hydrophobic pocket in pro-IL-18 through an exosite, caspase-4 interacts with charged residues in and near the tetrapeptide in the pro-domain of pro-IL-18. This mode of interaction is different from how caspases recognize GSDMD and pro-IL-1β. Recognition via the conserved hydrophobic exosite is necessary and sufficient to mediate cleavage of GSDMD, which occurs in a tetrapeptide-independent manner[7]. Conversely, pro-IL-1β cleavage by caspase-1 appears to be largely independent of exosite residues in the caspase[16]. We observed different conformations of caspase-4-bound pro-IL-18 versus free cleaved IL-18, and caspase-4 is unable to bind to mature IL-18, suggesting that cleavage may trigger a conformational change in IL-18 and its release from the caspase. Our studies therefore reveal molecular insights into the catalytic mechanism of inflammatory caspases and may provide a framework for the design of inhibitors of caspase-4 and other inflammatory caspases as tools for research and drug candidates.

Our study also highlights a disconnect in the regulation of IL-18 between humans and mice. Caspase-4 homologues in rodents are unable to cleave pro-IL-18 efficiently, despite sharing almost 70% sequence identity with human caspase-4. Using our caspase-4–pro-IL18 structure as a blueprint, we mapped the regions that are responsible for these differential cleavage specificities to regions near the active site, which enabled us to engineer a caspase-11 variant with increased IL-18-converting enzyme activity. Thus, while caspase-4 proteins from other mammalian species can intrinsically link LPS detection to IL-1 family cytokine cleavage and release, mouse cells require inflammasomes to operate downstream from their caspase-4 homologues to execute this process. The implications of these biochemical and pathway differences for immunity at the organismal level remain to be uncovered. The organism-specific pathway differences uncovered in this study provide a mandate to consider the impact of species-specific innate immunity when designing preclinical animal models to test therapeutics that involve IL-18.

Online content

Any methods, additional references, Nature Portfolio reporting summaries, source data, extended data, supplementary information, acknowledgements, peer review information; details of author contributions and competing interests; and statements of data and code availability are available at https://doi.org/10.1038/s41586-023-06751-9.

1. Dinarello, C. A. Overview of the IL-1 family in innate inflammation and acquired immunity. *Immunol. Rev.* **281**, 8–27 (2018).
2. Bateman, G., Hill, B., Knight, R. & Boucher, D. Great balls of fire: activation and signalling of inflammatory caspases. *Biochem. Soc. Trans.* **49**, 1311–1324 (2021).
3. Chan, A. H. & Schroder, K. Inflammasome signaling and regulation of interleukin-1 family cytokines. *J. Exp. Med.* **217**, e20190314 (2020).
4. Shi, J. et al. Cleavage of GSDMD by inflammatory caspases determines pyroptotic cell death. *Nature* **526**, 660–665 (2015).
5. Kayagaki, N. et al. Caspase-11 cleaves gasdermin D for non-canonical inflammasome signalling. *Nature* **526**, 666–671 (2015).
6. Julien, O. & Wells, J. A. Caspases and their substrates. *Cell Death Differ.* **24**, 1380–1389 (2017).
7. Wang, K. et al. Structural mechanism for GSDMD targeting by autoprocessed caspases in pyroptosis. *Cell* **180**, 941–955 (2020).
8. Liu, Z. et al. Caspase-1 engages full-length gasdermin D through two distinct interfaces that mediate caspase recruitment and substrate cleavage. *Immunity* **53**, 106–114 (2020).
9. Shi, J., Gao, W. & Shao, F. Pyroptosis: gasdermin-mediated programmed necrotic cell death. *Trends Biochem. Sci.* **42**, 245–254 (2017).
10. Evavold, C. L. et al. The pore-forming protein gasdermin D regulates interleukin-1 secretion from living macrophages. *Immunity* **48**, 35–44 (2018).
11. Heilig, R. et al. The gasdermin-D pore acts as a conduit for IL-1β secretion in mice. *Eur. J. Immunol.* **48**, 584–592 (2018).
12. Xia, S. et al. Gasdermin D pore structure reveals preferential release of mature interleukin-1. *Nature* **593**, 607–611 (2021).
13. Barnett, K. C., Li, S., Liang, K. & Ting, J. P.-Y. A 360° view of the inflammasome: mechanisms of activation, cell death, and diseases. *Cell* **186**, 2288–2312 (2023).
14. Kagan, J. C., Magupalli, V. G. & Wu, H. SMOCs: supramolecular organizing centres that control innate immunity. *Nat. Rev. Immunol.* **14**, 821–826 (2014).
15. Thornberry, N. A. et al. A novel heterodimeric cysteine protease is required for interleukin-1 β processing in monocytes. *Nature* **356**, 768–774 (1992).
16. Devant, P., Cao, A. & Kagan, J. C. Evolution-inspired redesign of the LPS receptor caspase-4 into an interleukin-1β–converting enzyme. *Sci. Immunol.* **6**, eabh3567 (2021).
17. Bibo-Verdugo, B., Snipas, S. J., Kolt, S., Poreba, M. & Salvesen, G. S. Extended subsite profiling of the pyroptosis effector protein gasdermin D reveals a region recognized by inflammatory caspase-11. *J. Biol. Chem.* **295**, 11292–11302 (2020).
18. Faucheu, C. et al. A novel human protease similar to the interleukin-1 beta converting enzyme induces apoptosis in transfected cells. *EMBO J.* **14**, 1914–1922 (1995).
19. Kamens, J. et al. Identification and characterization of ICH-2, a novel member of the interleukin-1β-converting enzyme family of cysteine proteases. *J. Biol. Chem.* **270**, 15250–15256 (1995).
20. Shi, J. et al. Inflammatory caspases are innate immune receptors for intracellular LPS. *Nature* **514**, 187–192 (2014).
21. Rühl, S. & Broz, P. Caspase-11 activates a canonical NLRP3 inflammasome by promoting K^+ efflux. *Eur. J. Immunol.* **45**, 2927–2936 (2015).
22. Baker, P. J. et al. NLRP3 inflammasome activation downstream of cytoplasmic LPS recognition by both caspase-4 and caspase-5. *Eur. J. Immunol.* **45**, 2918–2926 (2015).
23. Kayagaki, N. et al. Non-canonical inflammasome activation targets caspase-11. *Nature* **479**, 117–121 (2011).
24. Wandel, M. P. et al. Guanylate-binding proteins convert cytosolic bacteria into caspase-4 signaling platforms. *Nat. Immunol.* **21**, 880–891 (2020).
25. Knodler, L. A. et al. Noncanonical inflammasome activation of caspase-4/caspase-11 mediates epithelial defenses against enteric bacterial pathogens. *Cell Host Microbe* **16**, 249–256 (2014).
26. Devant, P. & Kagan, J. C. Protocol to purify recombinant inflammatory caspases and assess their catalytic activity in vitro. *STAR Protoc.* **3**, 101848 (2022).
27. Holly, M. K. et al. *Salmonella enterica* infection of murine and human enteroid-derived monolayers elicits differential activation of epithelium-intrinsic inflammasomes. *Infect. Immun.* **88**, e00017-20 (2020).
28. Naseer, N. et al. *Salmonella enterica* Serovar Typhimurium induces NAIP/NLRC4- and NLRP3/ASC-independent, caspase-4-dependent inflammasome activation in human intestinal epithelial cells. *Infect. Immun.* **90**, e0066321 (2022).
29. Kobayashi, T. et al. The *Shigella* OspC3 effector inhibits caspase-4, antagonizes inflammatory cell death, and promotes epithelial infection. *Cell Host Microbe* **13**, 570–583 (2013).
30. Gritsenko, A. et al. Priming is dispensable for NLRP3 inflammasome activation in human monocytes in vitro. *Front. Immunol.* **11**, 565924 (2020).
31. Coll, R. C. et al. A small-molecule inhibitor of the NLRP3 inflammasome for the treatment of inflammatory diseases. *Nat. Med.* **21**, 248–255 (2015).
32. Reyes Ruiz, V. M. et al. Broad detection of bacterial type III secretion system and flagellin proteins by the human NAIP/NLRC4 inflammasome. *Proc. Natl Acad. Sci. USA* **114**, 13242–13247 (2017).
33. Tsutsumi, N. et al. The structural basis for receptor recognition of human interleukin-18. *Nat. Commun.* **5**, 5340 (2014).
34. Krissinel, E. & Henrick, K. Inference of macromolecular assemblies from crystalline state. *J. Mol. Biol.* **372**, 774–797 (2007).
35. Jumper, J. et al. Highly accurate protein structure prediction with AlphaFold. *Nature* **596**, 583–589 (2021).

Methods

No statistical methods were used to predetermine sample size. Experiments were not randomized, and investigators were not blinded during experiments and during outcome assessment. Statistical analyses were performed using GraphPad Prism (v.6.01). Statistical tests are indicated in the figure legends.

Ligand and chemical reconstitution

E. coli LPS (serotype O:111 B4) was purchased from Enzo Biosciences as a ready-to-use stock solution of 1 mg ml^{-1} or purchased from Invivogen and reconstituted in ultrapure water at a stock concentration of 1 mg ml^{-1} and used at a working concentration of 1 μg ml^{-1}. Pam3CSK4 was purchased from Invivogen and reconstituted in ultrapure water at a stock concentration of 1 mg ml^{-1} and used at a working concentration of 1 μg ml^{-1}. MCC950 (from Invivogen) was resuspended in sterile DMSO to a concentration of 20 mM and used at a final concentration of 10 μM. Recombinant human M-CSF (CHO expressed, carrier-free) was bought from R&D Systems and dissolved in sterile PBS pH 7.4 (stock concentration of 100 μg ml^{-1}). Phorbol-12-myristate-13-acetate (PMA; from Sigma-Aldrich) was reconstituted at 50 μg ml^{-1} in DMSO. Ac-WEHD-pNA was from Enzo Biosciences and the stock solution was prepared at 20 mM in DMSO. BS3 was purchased from Thermo Fisher Scientific in a no-weigh format (2 mg per aliquot) and prepared freshly before each use in ultrapure water at 25 mM and used at 1 mM.

Antibodies for immunoblotting

Primary antibodies for immunoblotting were purchased from the following vendors: monoclonal rabbit anti-human caspase-1, polyclonal rabbit anti-human caspase-4, monoclonal rabbit anti-human caspase-5, monoclonal rabbit anti-MYC-tag, monoclonal mouse anti-MYC-tag and monoclonal rabbit anti-mouse IL-18, monoclonal rabbit anti-human GSDMD (all from Cell Signaling); monoclonal mouse anti-caspase-4 (Enzo Biosciences), monoclonal mouse anti-mouse and human NLRP3 (Adipogen), polyclonal rabbit anti-human IL-18 (MBL), monoclonal rabbit anti-cleaved GSDMD-NT and monoclonal rabbit anti-mouse IL-18 (all from Abcam); monoclonal rat anti-actin and monoclonal rat anti-caspase-11 (both from BioLegend); monoclonal mouse anti-canine IL-18 (R&D Systems), polyclonal rabbit anti-human IL-1β, polyclonal rabbit anti-mouse IL-1β (both from Genetex), monoclonal mouse-anti-actin (Sigma-Aldrich). All primary antibodies were used at a dilution of 1:1,000 in PBS pH 7.4 + 0.02% Tween-20 and 5% BSA, except for mouse anti-actin, which was used at 1:5,000 in the same buffer.

Constructs

Constructs encoding N-terminally MYC-tagged full-length human caspase-1, caspase-4 and mouse caspase-11 in the pMSCV-IRES-eGFP vector were described previously[16] and are available from Addgene (183359, 183358, 183356). Sequences encoding full-length human caspase-5 with an N-terminal MYC-tag were ordered from Integrated DNA technologies and cloned into the pMSCV-IRES-EGFP vector using the NotI and SalI restriction sites. Expression plasmid for caspase-1 p20 and p10 were provided by S. Xiao. Constructs for bacterial expression of the catalytic domains of human caspase-4 and mouse caspase-11, human and mouse pro-IL-18 were described previously[16] and deposited at Addgene (Addgene, 183381, 183382, 183389, 183390). For expression in insect cells, the sequence for human pro-IL-18 was cloned into pFastBac HTb using the BamHI and XhoI restriction sites. For retroviral transduction, an N-terminal MYC-tag and a C-terminal Flag-tag were added to human pro-IL-18 by PCR and the sequence was cloned into the pMSCV-IRES-eGFP vector using the NotI and SalI restriction sites. Sequences encoding the catalytic domains of human caspase-5 (amino acids 133–434) as well as the catalytic domains of caspase-4 homologues from lemur *Microcebus murinus*, sheep *Ovis aries*, rabbit *Oryctolagus cuniculus* and dog *Canis lupus familiaris* were subcloned by PCR from full-length sequences and cloned into pET28a with an N-terminal His_6-tag and a TEV cleavage site using the BamHI and EcoRI cleavage sites. Full-length sequences for these caspase-4 homologues are available at Addgene (Addgene, 183365, 183374, 183375, 183376). cDNAs encoding the catalytic domain of rat caspase-11, pro-IL-18 homologues from all of the mammalian species listed above as well as human pro-IL-1β, pro-IL-1α, pro-IL-33, pro-IL-36α, pro-IL-36β, pro-IL-36γ and pro-IL-37 were synthesized by Integrated DNA Technologies and cloned into pET28a with an N-terminal His-tag and TEV cleavage site. C-terminal MYC-tags were added to cytokine sequences by PCR. All point mutations and deletions were introduced using the Q5 site-directed mutagenesis kit (NEB) according to the manufacturer's instructions. The sequence encoding the p20 subunit of caspase-4 (with the C258A mutation) or the p10 subunit of caspase-4 were subcloned from the full-length sequence by PCR and cloned into a pET28a vector (+N-terminal His-tag and TEV cleavage site) or a modified pET16b vector (without tags), respectively. The modified pET16b vector was a gift from P. Kranzusch. All constructs generated in this paper were sequence-confirmed using Sanger sequencing.

Cell lines

All cells were cultured in humidified incubators at 37 °C and 5% CO_2. iBMDMs were generated at the Jonathan Kagan Laboratory from the bone marrow of female WT C57BL/6J or *Nlrp3*-KO mice (B6.129S6-Nlrp3tm1Bhk/J)[36]. iBMDMs and HEK293T cells were cultured in DMEM supplemented with 10% fetal bovine serum (FBS), penicillin–streptomycin, L-glutamine and sodium pyruvate, hereafter referred to as complete DMEM (cDMEM) and cultured in tissue-culture-treated 10 cm dishes or T175 tissue culture flasks (Corning). iBMDMs and HEK293T cells were passaged using sterile PBS pH 7.4 + 4 mM EDTA or 0.25% trypsin + EDTA (Gibco), respectively. WT THP1 cells were obtained from ATCC and *NLRP3*-KO THP1 cells were obtained from Invivogen. THP1 cells were cultured in RPMI supplemented with 10% FBS, penicillin–streptomycin, L-glutamine and sodium pyruvate, hereafter referred to as complete RPMI (cRPMI) and cultured in suspension culture in T75 or T175 tissue culture flasks (Corning). For differentiation into macrophages, THP1 cells were treated with 100 ng ml^{-1} of PMA for 18–24 h. Sf9 insect cells were purchased from Thermo Fisher Scientific and grown in suspension culture in sterile glass flasks in Hyclone SFX insect cell medium at 28 °C under ambient CO_2 with shaking at 120 rpm. All of the cell lines were verified by the manufacturer's website and the identities were checked on the basis of their morphological features. THP1 cells tested negative for mycoplasma contamination using the MycoStrip kit (Invivogen).

Primary cell culture

Buffy coats from healthy human donors were purchased from BioIVT. Primary cells were cultured in cRPMI. Blood was diluted at a 1:1 ratio with sterile PBS pH 7.4 + 2.5 mM EDTA before layering 30 ml of diluted blood over 15 ml of FiColl Paque PLUS density-gradient medium (GE Healthcare). Density-gradient centrifugation was performed at 800*g* for 35 min at 20 °C at lowest acceleration and without breaks. Total peripheral blood mononuclear cells were collected from the interphase and washed twice with magnetic-activated cell sorting (MACS) buffer (PBS pH 7.4, 2.5 mM EDTA, 1% FBS). Red blood cells were lysed by resuspending the pellet in 10 ml ACK lysis buffer and incubating for 5 min at room temperature. After a final wash step in MACS buffer, CD14$^+$ PBMCs were isolated by MACS. Cells were resuspended in 800 μl of MACS buffer mixed with 200 μl of human CD14 microbeads (Miltenyi). After incubation on ice in the dark for 15 min, cells were washed one more time in 20 ml of MACS buffer, resuspended in 2.5 ml and poured over an LS column (Miltenyi) placed into a magnetic holder and pre-equilibrated with 2.5 ml of MACS buffer. The column was washed three times with 2.5 ml of MACS buffer. The column was then removed from the magnetic holder and CD14$^+$ PBMCs were eluted

in 5 ml of MACS buffer using the provided plunger. Cells were then seeded in T75 cell culture flasks (20×10^6 $CD14^+$ PBMCs per flask) in 15 ml cRPMI supplemented with 30 ng ml^{-1} of recombinant human M-CSF (R&D Systems) for 6 days. The medium was replenished with fresh cRPMI containing M-CSF every 2–3 days.

Generation of KO cell lines using CRISPR–Cas9 technology

CRISPR KO cell lines were generated by electroporation of in vitro assembled ribonucleoproteins (RNPs) consisting of synthetic sgRNAs and recombinant Cas9 protein (Alt-R *Streptococcus pyogenes* HiFi Cas9 nuclease from IDT) using the Neon transfection system (Thermo Fisher Scientific). RNPs were assembled by mixing 0.3 µl of Cas9 protein (62 µM) with 0.5 µl of sgRNA (ordered from IDT and resuspended in nuclease-free water at a concentration of 100 µM) and incubated at room temperature for 15–20 min. A total of 1.2×10^6 THP1 cells was resuspended in 12 µl of T buffer, mixed with the assembled RNPs and electroporated using a 10 µl electroporation pipette tip with two 10 ms pulses at a voltage of 1,400 V. Cells were then dispensed directly into a six-well plate containing 3 ml of cRPMI and cultured for 3–5 days before assessing bulk KO efficiency by immunoblotting. These cell lines were further single-cell cloned by limited serial dilution in single-cell cloning medium (40% THP1 conditioned medium, 40% RPMI, 20% FBS) to obtain clonal KO cell populations with complete ablation of the target protein. sgRNA sequences were pre-designed by IDT (non-target sgRNA: AAAUGUGAGAUCAGAGUAAU; *CASP1* sgRNA, CGGCTTGACTTGT CCATTAT; *CASP4* sgRNA, AGGGATTCCAACACCTTAAG; *IL18* sgRNA, CAAATAGAGGCCGATTTCCT).

Retroviral transduction

HEK293T cells were used as packaging cells for retroviral vectors. For the production of retroviral particles, 2.5×10^6 HEK293T cells were seeded into a 10 cm cell culture dish. After overnight incubation at 37 °C, cells were transfected with 10 µg of pMSCV-IRES-eGFP encoding the protein of interest, 6 µg of pCL-ECO and 3 µg of pCMV-VSVG using Lipofectamine 2000 (Thermo Fisher Scientific) according to the manufacturer's instructions. After 18–24 h at 37 °C, the medium was changed to 6 ml of fresh cRPMI (for transduction of THP1 cells) and the virus-containing supernatant was collected 24 h after the medium change. The supernatants were clarified from cellular debris by centrifugation (400*g*, 5 min) and filtered through a 0.45 µm PVDF syringe filter. A total of 1×10^6 THP1 cells was resuspended in 4.5 ml of viral supernatant supplemented with Polybrene (1:2,000; EMD Millipore) and plated in a six-well plate followed by centrifugation for 1 h at 1,250*g* and 30 °C. This procedure was performed twice on two consecutive days to maximize the transduction efficiency. GFP^+ cells were sorted twice on the FACSAria or FACSMelody cell sorter (BD Biosciences) to obtain cell lines with stable and homogenous expression of the target protein. Transgene expression was confirmed by immunoblotting using rabbit anti-MYC-tag or mouse anti-MYC-tag primary antibodies (both from Cell Signaling Technologies).

Recombinant protein expression and purification

Expression and purification of caspase catalytic domains and IL-1 family cytokine substrates for in vitro cleavage assays were expressed in bacteria and purified as described previously[16,26]. Chemically competent Rosetta (DE3) pLysS cells (EMD Millipore) were transformed with the pET28 plasmid encoding the protein of interested and plated on LB agar plates with kanamycin (25 µg ml^{-1}). Overnight precultures were inoculated with a single colony and grown at 30 °C and 250 rpm in 2× YT medium containing kanamycin (25 µg ml^{-1}) and chloramphenicol (50 µg ml^{-1}). Individual expression cultures of 50 to 500 ml were inoculated with overnight cultures at a ratio of 1:100 and incubated at 37 °C and 250 rpm until the optical density at 600 nm (OD_{600}) reached a value between 0.7 and 0.8. After a cooling step on ice for 15 min, protein expression was induced by adding isopropyl-β-D-thiogalactopyranoside (IPTG) to a final concentration of 0.25 mM, and expression was allowed to proceed overnight at 18 °C. Bacterial pellets were collected by centrifugation (5,000*g* for 20 to 30 min at 4 °C) and stored at −20 °C if not immediately used for protein purification. To purify recombinant proteins, bacterial pellets were resuspended in resuspension buffer (25 mM HEPES-NaOH (pH 7.4), 150 mM NaCl and 10 mM imidazole) and lysed by ultrasonication. Cell lysates were clarified by centrifugation (30–45 min, 20,000*g*, 4 °C) and filtered through a 0.22 µm syringe filter before pouring them into a gravity-flow column containing a bed of nickel–itrilotriacetic acid (Ni-NTA) agarose beads (Qiagen). The beads were washed with at least 10 bed volumes of wash buffer (25 mM HEPES (pH 7.4), 400 mM NaCl and 25 mM imidazole) and the bound protein was eluted stepwise in resuspension buffer supplemented with 40 to 250 mM imidazole. The elution fractions were analysed using SDS–PAGE followed by InstantBlue staining (Expedeon) to identify the fractions containing proteins of interest and confirm autocatalytic processing of caspase catalytic domains into active p20 and p10 subunits. The fractions containing the protein of interest were pooled and buffer-exchanged into SEC buffer (25 mM HEPES (pH 7.4), 150 mM NaCl) using a PD-10 desalting column (GE Healthcare). Pro-IL-18 variants used for binding assays were further purified by SEC using the BioRad NGC Quest10 Chromatography system equipped with the Superdex 200 Increase 10/300 column in SEC buffer. The peak fractions containing the protein of interest were identified by SDS–PAGE and InstantBlue staining and combined. Finally, the protein was concentrated by centrifugal ultrafiltration using an Amicon Ultra-15 centrifugal filter unit with a 10 kDa cut-off (EMD Millipore). Glycerol was added to a total concentration of 10% and aliquots were snap-frozen in liquid nitrogen and stored at −80 °C.

For the expression of catalytically inactive caspase-4-p20/p10 complexes for binding assays and structural studies, chemically competent Rosetta (DE3) cells (EMD Millipore) were co-transformed with a pET28a plasmid encoding the N-terminally His-tagged large p20 subunit (with a C258A mutation) and a pET16b plasmid encoding the untagged p10 subunit and plated onto LB agar plates with 25 µg ml^{-1} kanamycin and 100 µg ml^{-1} ampicillin. Overnight precultures were inoculated with a single colony and grown at 30 °C and 250 rpm in 2× YT medium containing kanamycin (25 µg ml^{-1}), ampicillin (100 µg ml^{-1}) and chloramphenicol (50 µg ml^{-1}). Then, 500 ml of 2× YT was inoculated with overnight cultures at a ratio of 1:100 and incubated at 37 °C and 250 rpm until the OD_{600} reached a value of between 0.7 and 0.8. After cooling on ice for 15 min, protein expression was induced by IPTG to a final concentration of 0.25 mM, and expression was allowed to proceed overnight at 18 °C. Bacterial pellets were collected by centrifugation (5000*g* for 15 min at 4 °C), washed once with PBS, pH 7.4, and stored at −20 °C if not immediately used for protein purification. For purification, the bacterial pellets were resuspended in resuspension buffer and lysed by ultrasonication. Cell lysates were clarified by centrifugation (30–45 min, 20,000*g*, 4 °C) and filtered through a 0.22 µm syringe filter before pouring them into a gravity-flow column containing a bed of Ni-NTA agarose beads. The beads were washed with at least 10 bed volumes of wash buffer and the bound protein was eluted in resuspension buffer supplemented with 250 mM imidazole. The proteins were further purified by SEC using the BioRad NGC Quest10 Chromatography system equipped with the Superdex 200 Increase 10/300 column in SEC buffer. Peak fractions containing the protein of interest were identified by SDS–PAGE and InstantBlue staining (Expedeon), pooled and protein was concentrated by centrifugal ultrafiltration using Amicon Ultra-15 centrifugal filter unit with a 10 kDa cut-off (EMD Millipore). Glycerol was added to a total concentration of 10% and aliquots were snap-frozen in liquid nitrogen and stored at −80 °C.

For expression of human pro-IL-18 and mature IL-18 in insect cells, chemically competent DH10Bac cells (Thermo Fisher Scientific) were transformed with a pFastBac vector encoding the protein of interest and cells were plated on LB agar plates supplemented with 25 µg ml^{-1} kanamycin, 10 µg ml^{-1} tetracycline, 7 µg ml^{-1} gentamycin, 50 µg ml^{-1} X-Gal

and 40 μg ml^{-1} IPTG and incubated for 24–48 h at 37 °C for blue/white screening. A total of 20 ml of LB medium with 25 μg ml^{-1} kanamycin, 10 μg ml^{-1} tetracycline, 7 μg ml^{-1} gentamycin was inoculated with one positive (white) colony and incubated overnight at 37 °C and 250 rpm. Bacmid DNA was isolated using buffer components from the GeneJET Plasmid Miniprep kit (Thermo Fisher Scientific) and precipitated using isopropanol. The DNA pellet was washed once with 70 % ethanol, air dried and resuspended in 40 μl of sterile, ultrapure water. A total of 10 μl of water containing bacmid DNA was diluted with 100 μl of Hyclone SFX insect cell medium. CellFectin II (10 μl; Thermo Fisher Scientific) transfection reagent was mixed with 100 μl of medium and added to the DNA mixture. After incubating at room temperature for 30 min, 100 μl of the transfection mix was added dropwise to 0.8×10^6 Sf9 cells seeded in the wells of a six-well plate in 3 ml of medium. Routinely, two wells were used for each construct. After 3–4 days of incubation at 28 °C, the baculovirus-containing supernatant was collected, filtered using a 0.45 μm syringe filter and stored at 4 °C. To amplify the initial P1 virus, Sf9 cells were grown at a density of 1.0×10^6 cells per ml in a total volume of 25 ml, infected with 2 ml of the initial virus and incubated at 28 °C and 120 rpm. After 3 days, virus was collected by centrifuging the cells at 1,000*g* for 10 min and taking off the baculovirus-containing supernatant, which was then passed through a 0.45 μm syringe filter and stored at 4 °C. For protein expression, *Sf* 9 cells were grown to a density of 1.5×10^6 cells per ml in a suspension culture with a volume of up to 1 l in a 2.8 l Fernbach flask, infected with 1% (v/v) of the amplified virus and incubated at 28 °C and 120 rpm. Cells were collected by centrifugation (1,000*g*, 15 min), 48–72 h after a proliferation arrest occurred. Cell pellets were frozen in liquid nitrogen and stored at −20 °C until protein purification. For purification, insect cell pellets were resuspended in resuspension buffer and lysed by ultrasonication. Cell lysates were clarified by centrifugation (30–45 min, 20,000*g*, 4 °C) and filtered through a 0.22 μm syringe filter before pouring them into a gravity-flow column containing a bed of Ni-NTA agarose beads. The beads were washed with at least 10 bed volumes of wash buffer and the bound protein was eluted in resuspension buffer supplemented 250 mM imidazole. The proteins were further purified by SEC using the BioRad NGC Quest10 Chromatography system equipped with the Superdex 200 Increase 10/300 column in SEC buffer. The peak fractions containing the protein of interest were identified by SDS–PAGE and InstantBlue staining (Expedeon), pooled and protein was concentrated by centrifugal ultrafiltration using Amicon Ultra-15 centrifugal filter unit with a 10 kDa cut-off (EMD Millipore). Glycerol was added to a total concentration of 10% and aliquots were snap-frozen in liquid nitrogen and stored at −80 °C.

The human caspase-1 catalytic domain was expressed and purified as described previously[37]. In brief, two non-tagged p20 and p10 subunits were expressed as inclusion bodies in *E. coli* BL21 (DE3), respectively. The two subunits were assembled by denaturing, refolding and further purified by HiTrap SP cation-exchange chromatography (GE Healthcare Life Sciences).

Human GSDMD was purified as described previously[38]. Protein concentrations were determined by measuring the absorbance of the protein solution at 280 nm on a Nanodrop device and corrected by the protein-specific extinction coefficient.

Assembly of caspase-4–pro-IL-18 complex for structural studies

Purified caspase-4-p20/p10 with an inactivating C258A mutation was mixed with insect-cell-purified human pro-IL-18 at a molar ratio of about 1:2 in SEC buffer and incubated at 37 °C for 20 min. The mixture was then centrifuged at 12,000*g* for 5 min at 4 °C to spin down any precipitate that may have formed, and fractionated by SEC using the BioRad NGC Quest10 Chromatography system equipped with a Superdex 200 Increase 10/300 column in SEC buffer. The fractions containing the assembled complex of caspase-4 and pro-IL-18 (indicated by a shift in retention volume and confirmed by SDS–PAGE and InstantBlue staining) were combined and the chemical cross-linker BS3 (Thermo Fisher Scientific) was added at a final concentration of 1 mM. After incubation on ice for 1 h, BS3 was quenched by adding 50 mM Tris (pH 7.4). For cross-linking mass-spectrometry, BS3 was quenched using 100 mM hydroxylamine. The protein complex was concentrated by centrifugal ultrafiltration using the Amicon Ultra-15 centrifugal filter unit with a 10 kDa cut-off (EMD Millipore) and again purified by SEC (Superdex 200 Increase 10/300) in SEC buffer.

Negative-stain electron microscopy

The peak fractions of SEC containing cross-linked caspase-4–pro-IL-18 were diluted to a final concentration of around 0.015 mg ml^{-1} for negative-stain electron microscopy. A total of 6 μl sample was added to each copper grid with carbon support film (Electron Microscopy Sciences) that had been glow-discharged for 30 s using the Pelco EasyGlow (Ted Pella) instrument. After 1 min, the sample was stained twice with 6 μl of 2% uranyl acetate solution (Electron Microscopy Sciences) for 30 s each, with removal of excess buffer using filter papers (Whatman) after each round of staining. The negatively stained grids were imaged on a transmission electron microscope (Joel JEM1400) at 120 keV.

Cryo-EM data collection

The peak fractions of cross-linked caspase-4–pro-IL-18 from SEC were concentrated to about 0.22 mg ml^{-1} for cryo-EM grid preparation. A total of 3.3 μl sample was placed onto each glow-discharged cryo-EM grid (Quantifoil R1.2/1.3 gold grid with 400 mesh, Electron Microscopy Sciences) before being blotted for 3–5 s under 100% humidity at 4 °C and plunged into liquid ethane using the Mark IV Vitrobot (Thermo Fisher Scientific). Before data collection, all of the grids were pre-screened and optimized at the Harvard Cryo-EM Center for Structural Biology or at cryo-EM facility of University of Massachusetts (UMASS) to check the ice thickness and particle distribution.

The final datasets were collected at UMASS on the Titan Krios electron microscope (Thermo Fisher Scientific) equipped with a K3 Summit direct electron detector (Gatan) and a post-column energy filter (Gatan). In total, 5,934 videos were collected under the super-resolution mode at ×105,000 magnification (0.4125 Å per pixel) with a defocus range between −1.0 and −2.5 μm, and three shots were recorded for each hole per stage movement. For each video stack with 40 frames, the total dose was 60.8 electrons per Å^2. SerialEM was used for automated data collection[39].

Cryo-EM data processing

The computer support and software for data processing was provided by SBGrid consortium[40]. Raw videos were corrected by gain reference and beam-induced motion, and binned by twofold with or without dose weighting using the Relion v.3.08 implementation of the MotionCor2 algorithm[41]. The motion-corrected micrographs were imported into CryoSPARC[42]. Patch CTF-estimation was performed to determine the local defocus values in each micrograph. Blob picking on a random subset of 500 micrographs was used to generate a template that was used to pick a total of 10,802,676 particles. Multiple rounds of 2D classification were performed, resulting in 1,234,038 good particles that were used for ab initio 3D reconstruction. Heterogeneous refinement was first performed to classify the particles into five classes. The dominant class with 229,147 particles was further processed by homogeneous refinement with C_2 symmetry to achieve a final map at a corrected resolution of 3.2 Å. The reported resolutions under different processing conditions were estimated on the basis of the gold-standard Fourier shell correlation (FSC) = 0.143 criterion. The cryo-EM map was further sharpened by applying a negative *B* factor using automated procedures in Phenix[43]. Local resolution estimation of all of the cryo-EM maps was performed in Phenix[44].

Model fitting and building

The crystal structure of caspase-4 dimer (Protein Data Bank (PDB): 6KMZ)[7] and mature IL-18 (PDB: 3WO2)[33] were used as initial templates for

map fitting in the UCSF ChimeraX software[45]. The caspase-4–pro-IL-18 complex structure was refined by real space refinement and validated by model validation in Phenix. Protein–protein interaction analysis was conducted using the PISA webserver[34]. Per-residue Cα–Cα distances in the caspase-4–pro-IL-18 complex were calculated using the Distances function in UCSF ChimeraX, and used to correlate with cross-linking MS data. To generate the model of the caspase-11–pro-IL-18 complex, the crystal structure of caspase-11 (PDB: 6KN1)[7] was fitted into the electron density and aligned with our caspase-4 model in UCSF ChimeraX.

AlphaFold implementation in the ColabFold notebooks running on Google Colaboratory[35,46] was used to predict the structure for pro-IL-18 alone. The top five models predicted by AlphaFold were aligned and checked for consistency. The pLDDT (predicted local distance difference test, 0–100 with 100 being the best) score computed by AlphaFold was used to indicate the reliability of prediction.

Cross-linking MS analysis

BS3-cross-linked caspase-4–pro-IL-18 complex was purified as described above. For analysis of pro-IL-18 before binding to caspase-4, human pro-IL-18 purified from insect cells was diluted to 0.34 mg ml^{-1} in SEC buffer and cross-linked with 1 mM of BS3 on ice for 1 h. BS3 was then quenched with 100 mM hydroxylamine for 10 min on ice. Lyophilized samples were resuspended in a buffer containing 8 M urea and 50 mM EPPS, pH 8.3 and reduced for 0.5 h with 10 mM TCEP. Proteins were alkylated with 30 mM iodoacetamide in the dark for 1 h, before quenching with 50 mM β-mercaptoethanol. The samples were then diluted eightfold with 50 mM EPPS, pH 8.3, to dilute out urea and digested with trypsin overnight at 37 °C (Promega; 1:25 ratio of enzyme:substrate). Then, 10% formic acid was added to a final pH of 2. The samples were desalted using stage tips with Empore C18 SPE extraction discs (3M) and dried under a vacuum. The peptides were then reconstituted in 5% formic acid and 5% acetonitrile and analysed using the Orbitrap Eclipse mass spectrometer (Thermo Fisher Scientific) coupled to an EASY-nLC 1200 (Thermo Fisher Scientific) ultra-high-pressure liquid chromatography pump, as well as a high-field asymmetric waveform ion mobility spectrometry (FAIMS) FAIMSpro interface. Peptides were separated on an in-house column with a 100 µM inner diameter and packed with 30 cm of Accucore C18 resin (2.6 µm, 150 Å, Thermo Fisher Scientific), in a gradient of 5–35% (acetonitrile, 0.125% formic acid) over 120 min at about 500 nl min^{-1}. The instrument was operated in data-dependent mode. FTMS1 spectra were collected at a resolution of 120,000, with an automatic gain control target of 4×10^5, and a maximum injection time of 50 ms. The most intense ions were selected for tandem MS for 1.5 s in top-speed mode, while switching among three FAIMS compensation voltages (−40, −60 and −80 V). Previously investigated precursors were excluded using a dynamic exclusion window of 90 s. MS2 precursors were isolated with a quadrupole mass filter set to a width of 0.7 Th and analysed by FTMS2, with the Orbitrap operating at 30,000 resolution, an automatic gain control target of 125,000 and a maximum injection time of 150 ms. Precursors were then fragmented by high-energy collision dissociation at a 30% normalized collision energy.

Mass spectra were processed and searched using the PIXL search engine[47] against a sequence database containing most abundant contaminants from *Spodoptera frugiperda* and *E. coli* in addition to caspase and IL-18 construct sequences with a precursor tolerance of 15 ppm and fragment ion tolerance of 10 ppm. Methionine oxidation was set as a variable modification. The mass of BS3 was set as +156.0786 or +138.0681 for mono-linked or cross-linked, respectively. All cross-linked searches included the 50 most abundant protein sequences to ensure sufficient statistics for estimating the false-discovery rate. Matches were filtered to 1% false-discovery rate at the unique peptide level using linear discriminant features[47].

In vitro protein cleavage assay

Proteolytic cleavage of purified full-length protein substrates by caspases was assessed as described previously[26]. Twofold dilution series of the indicated recombinant caspase was incubated with substrate protein at a final concentration of 50 nM in 40 µl of caspase assay buffer (10 mM PIPES pH 7.2, 10% sucrose, 10 mM DTT, 100 mM NaCl, 1 mM EDTA, 0.1% CHAPS) for 30 min at 37 °C. The reactions were stopped by adding 10 µl of 5× SDS loading dye with reducing agent and boiling at 65 °C for 10 min. Cleavage products were separated by SDS–PAGE and analysed by immunoblotting using rabbit anti-human IL-18 (MBL), rabbit anti-mouse IL-18 (Abcam), rabbit anti-MYC (Cell Signaling), rabbit anti-human IL-1β (Genetex) or rabbit anti-GSDMD (Cell Signaling) primary antibodies. Band intensities were quantified using ImageJ to determine half-maximal effective concentration values (EC_{50}) and catalytic efficiencies were calculated using the following equation:

$$\frac{k_{cat}}{K_m} = \frac{\ln(2)}{(EC_{50} \times t)}$$

In vitro peptide-cleavage assay

For peptide-cleavage assays, recombinant caspase-4 p20/p10 carrying the indicated mutations was first diluted to a concentration of 1 µM in caspase assay buffer. To start the reaction, 50 µl of the diluted caspase was then mixed with 50 µl of the chromogenic tetrapeptide substrate Ac-WEHD-pNA (100 µM final concentration) in the same buffer (final concentration of caspase was 500 nM in a total volume of 100 µl) in a clear 96-well plate. The absorbance at a wavelength of 405 nm was measured every 20 s for 30 min using the Tecan Spark plate reader with temperature control set to 37 °C. The substrate solution was prewarmed to 37 °C before adding to the caspase to ensure homogeneous assay conditions.

LPS electroporation

The Neon transfection system (Thermo Fisher Scientific) was used to deliver LPS into the cytoplasm of cells. For priming, iBMDMs, THP1 macrophages or primary human macrophages were treated with 1 µg ml^{-1} of LPS for 4 h. Monocytic THP1s were primed with 1 µg ml^{-1} of Pam3CSK4 for 4 h. Mouse iBMDMs or human primary macrophages were resuspended in R buffer at a density of 10×10^6 cells per ml in a volume of 120 µl per sample. THP1 cells (both monocytes and macrophages) were resuspended in T buffer at a density of 250×10^6 cells per ml in a volume of 12 µl per sample. LPS or sterile PBS pH 7.4 (as negative control) was mixed with the cell suspension (1 µg of LPS per 1×10^6 iBMDMs or primary macrophages, 0.5 µg of LPS per 1×10^6 THP1 cells) before aspirating the cell suspension into the Neon electroporation pipette equipped with a 100 µl tip (for iBMDMs and primary macrophages) or 10 µl tip (for THP1 cells) and performing electroporation with two pulses with a pulse width of 10 ms each and a voltage of 1,400 V. Cells were then dispensed into an appropriate cell culture medium (5×10^5 cells per ml in cDMEM for iBMDMs and 3.33×10^5 cells per ml in cRPMI for human primary macrophages or 1.25×10^6 cells per ml in cRPMI for THP1 cells). THP1 cells or iBMDMs were then plated in 96-well plates (200 µl per well in duplicate wells for each condition) for LDH assay and ELISA or 12-well plates (2 ml per well and one well per condition) for IL-1 cytokine immunoprecipitation experiments and incubated for 2 h. Primary human macrophages were seeded in 12-well and 6-well plates (in 1.5 ml or 3 ml of medium, respectively, and one well per condition) and LDH assay, ELISA and cytokine pull-downs were performed on the supernatants after 2 h.

Bacterial infections

The *Salmonella* strain deficient for flagellin (SL1344 *fliC/fljB*) was a gift from I. Brodsky and infections were performed as described previously

with minor modifications[48]. Bacteria were streaked onto LB agar plates containing 25 μg ml^{-1} kanamycin, grown overnight at 37 °C and the plates were stored at 4 °C for up to 2 weeks. Overnight cultures (3 ml LB + 25 μg ml^{-1} kanamycin and 25 μg ml^{-1} chloramphenicol) were inoculated with a single bacterial colony and grown at 37 °C while shaking at 250 rpm. The next morning, the bacterial culture was diluted into high-salt LB (3 ml LB + 100 μl of overnight culture + 78 μl of sterile 5 M NaCl) and incubated for another 3 h at 37 °C without shaking. A total of 1×10^5 THP1 cells was seeded into 96-well plates cRPMI without penicillin–streptomycin (duplicate wells for each condition) and differentiated overnight with 100 ng ml^{-1} PMA. Bacteria were washed once cRPMI without penicillin–streptomycin and added to cells at a multiplicity of infection of 100 in 200 μl cRPMI without penicillin–streptomycin (based on an assumption of 5×10^8 CFU ml^{-1} at OD = 1). Where indicated, MCC950 was present in the medium at a concentration of 10 μM. Synchronized infection was facilitated by spinning the plates at 500*g* for 5 min right after addition of bacteria-containing medium and cells were incubated at 37 °C under 5% CO_2. After 1 h, gentamicin was added to a final concentration of 100 μg ml^{-1} to kill extracellular bacteria. Cell culture supernatants for downstream analyses (LDH assay and ELISA) were collected at 24 h after infection.

LDH assay

Lytic cell death was quantified by the LDH-release assay using the CyQuant LDH cytotoxicity assay kit (Thermo Fisher Scientific). In a 96-well plate, 50 μl of cell-free supernatants was mixed with 50 μl of LDH assay buffer and incubated for 15–20 min at 37 °C in the dark. Absorbance at 490 nm and 680 nm was measured on the Tecan Spark plate reader and the signal was normalized to equally treated control samples in which cells were lysed using a detergent-containing lysis buffer.

Cytokine measurements by ELISA

Cytokine release into the supernatants of cell was assessed by ELISA using the IL-1β mouse uncoated ELISA kit (Thermo Fisher Scientific), the Total human IL-18 DuoSet kit (R&D Systems) and the Mouse IL-18 ELISA kit (MBL), respectively, according to the manufacturer's protocols. To quantify IL-18 levels in combined supernatant and lysate samples, cells were first lysed by adding the detergent-containing lysis buffer provided as part of the CyQuant LDH cytotoxicity assay kit (Thermo Fisher Scientific) directly to the wells (at 1:10 ratio) before performing ELISA analysis. We confirmed that all of the ELISA kits used in this study show a strong preference for the cleaved form over the uncleaved form of the cytokine to be measured.

Immunoprecipitation of IL-1 cytokines from cell culture supernatants

Supernatants from 0.5–5.0 × 10^6 cells (cell number consistent within each individual experiment; generally mouse IL-1β and IL-18 were immunoprecipitated from the supernatants of 1×10^6 iBMDMs; human IL-1β and IL-18 were immunoprecipitated from the supernatants of at least 2.5×10^6 THP1 cells or 0.5–1.0 × 10^6 primary macrophages) stimulated as indicated were transferred into microcentrifuge tubes and depleted of cells and debris by centrifuging at 400*g* for 5 min. Cell-free supernatants were transferred into new tubes and rotated overnight at 4 °C in the presence of 0.5 μg of biotinylated goat anti-mouse IL-1β or goat anti-human IL-1β antibodies or 0.75 μg of detection antibodies from the human and mouse IL-18 ELISA kits (all from R&D Systems) and 20 μl neutravidin agarose beads (Thermo Fisher Scientific). IL-18-mutant proteins carrying C-terminal Flag tags were immunoprecipitated using 15 μl of anti-Flag matrix (Thermo Fisher Scientific). The remaining cells in the well were lysed in 1× SDS loading dye and served as lysate control. The beads were washed three times with PBS pH 7.4 before eluting bound proteins in 50 μl of 1× SDS loading dye. Immunoprecipitated and cell-associated cytokines were detected by immunoblotting using a rabbit anti-mouse IL-1β antibody, rabbit anti-human IL-1β antibody (both from Genetex), rabbit anti-human IL-18 antibody (MBL) or rabbit anti-mouse IL-18 (Cell Signaling). Cell-associated actin was detected as the loading control using a mouse anti-actin antibody from Sigma-Aldrich.

Assessment of GSDMD and pro-IL-18 cleavage in cells

Processing of pro-IL-18 and GSDMD in cells was analysed by immunoblotting using a rabbit anti-IL-18 antibody (MBL) or rabbit anti-GSDMD (Cell Signaling) or rabbit anti-cleaved NT-GSDMD monoclonal antibodies (Abcam). THP1 macrophages were electroporated with LPS as described above. To capture proteins present in both the cell lysate and the cell culture supernatant, cells were resuspended in 1 ml of serum-free Opti-MEM instead of cRPMI. After incubation for 2 h, the samples for immunoblotting were prepared by adding 250 μl of 5× SDS loading buffer directly to the well and heated to 65 °C for 10 min to fully denature the proteins.

Binding assays

To test whether two proteins form a stable complex, analytical SEC was performed. Catalytically inactive caspase-4-p20/p10 (with the indicated additional mutations) was mixed with pro-IL-18 (with the indicated mutations) at an equimolar concentration of 25 μM in SEC buffer. After incubation at 37 °C for 20 min, SEC was performed on a BioRad NGC Quest10 Chromatography system equipped with a Superdex 200 Increase 10/300 column in SEC buffer.

Thermodynamic parameters of binding between pro-IL-18 and caspase-4-p20/p10 were determined by ITC on a MicroCal ITC200 (Malvern Pananalytical). Proteins were buffer-exchanged into SEC buffer using PD-10 Desalting columns (Cytiva) right before the measurements to minimize buffer mismatch. The sample cell was filled with 25 μM of the indicated caspase-4-p20/p10 complex and the syringe was filled with pro-IL-18 at a concentration of 150–200 μM. After an initial delay period of 60 s, a total of 19 injections (first injection of 0.4 μl in 0.8 s, 2 μl in 4 s for residual injections) was performed while stirring at 750 rpm with a twisted paddle syringe at a constant temperature of 37 °C. The spacing between individual injections was 180 s with a filter period of 5 s. The reference power was set to 6 μcal s^{-1} and feedback mode/gain was set to high. Reference titration of pro-IL-18 into SEC buffer was performed on each experimental day. Peaks were fitted and integrated using Origin (v.7.0). If appropriate, integrations and the baseline were adjusted manually and data from the first injection and extreme outliers were removed. Data from reference experiments were subtracted to correct for the heat of dilutions. The binding heat was plotted in dependence of the molar ratio and thermodynamic parameters were obtained by fitting with a 'one set of sites' binding curve with at least 200 iterations.

Reporting summary

Further information on research design is available in the Nature Portfolio Reporting Summary linked to this article.

Data availability

All data and materials reported in the Article and its Supplementary Information are available on request. Raw data needed to recreate plots and uncropped gel images are accessible in the Supplementary Information. The electron density maps of caspase-4–pro-IL-18 at 3.2 Å have been deposited at the Electron Microscopy Data Bank (EMDB) under accession code EMD-40678. The atomic coordinates for caspase-4–pro-IL-18 have been deposited at the PDB under accession code 8SPB. Atomic coordinates for mature IL-18 and caspase-11 were downloaded from the PDB under accession codes 3WO2 and 6KN1, respectively. Source data are provided with this paper.

36. Evavold, C. L. et al. Control of gasdermin D oligomerization and pyroptosis by the Ragulator–Rag–mTORC1 pathway. *Cell* **184**, 4495–4511 (2021).
37. Roschitzki-Voser, H. et al. Human caspases in vitro: expression, purification and kinetic characterization. *Protein Expr. Purif.* **84**, 236–246 (2012).
38. Hu, J. J. et al. FDA-approved disulfiram inhibits pyroptosis by blocking gasdermin D pore formation. *Nat. Immunol.* **21**, 736–745 (2020).
39. Mastronarde, D. N. Automated electron microscope tomography using robust prediction of specimen movements. *J. Struct. Biol.* **152**, 36–51 (2005).
40. Morin, A. et al. Collaboration gets the most out of software. *eLife* **2**, e01456 (2013).
41. Zheng, S. Q. et al. MotionCor2: anisotropic correction of beam-induced motion for improved cryo-electron microscopy. *Nat. Methods* **14**, 331–332 (2017).
42. Punjani, A., Rubinstein, J. L., Fleet, D. J. & Brubaker, M. A. cryoSPARC: algorithms for rapid unsupervised cryo-EM structure determination. *Nat. Methods* **14**, 290–296 (2017).
43. Klaholz, B. P. Deriving and refining atomic models in crystallography and cryo-EM: the latest Phenix tools to facilitate structure analysis. *Acta Crystallogr. D* **75**, 878–881 (2019).
44. Adams, P. D. et al. PHENIX: a comprehensive Python-based system for macromolecular structure solution. *Acta Crystallogr. D* **66**, 213–221 (2010).
45. Goddard, T. D. et al. UCSF ChimeraX: meeting modern challenges in visualization and analysis. *Protein Sci.* **27**, 14–25 (2018).
46. Mirdita, M. et al. ColabFold: making protein folding accessible to all. *Nat. Methods* **19**, 679–682 (2022).
47. Mintseris, J. & Gygi, S. P. High-density chemical cross-linking for modeling protein interactions. *Proc. Natl Acad. Sci. USA* **117**, 93–102 (2020).
48. Wynosky-Dolfi, M. A. et al. Oxidative metabolism enables *Salmonella* evasion of the NLRP3 inflammasome. *J. Exp. Med.* **211**, 653–668 (2014).

Acknowledgements We thank D. Okin for providing primary cells and other members of the Kagan and Wu laboratories for discussions; T. Sam Xiao for the caspase-1 expression plasmid and I. Brodsky for the *Salmonella* strain; R. Walsh, S. Sterling. M. Mayer and S. Rawson for cryo-EM grid screening and data collection, and K. Song for cryo-EM grid screening and dataset collection; and the staff at SBGrid for software and computing support. This work was supported by NIH grants AI67993, AI116550 and P30DK34854 (to J.C.K.), AI124491 and AI139914 (to H.W.), a PhD fellowship by the Boehringer Ingelheim Fonds (to P.D.) and a postdoctoral fellowship from the Charles A. King Trust (to Y.D.). We acknowledge the International Union of Crystallography on the occasion of its 75th anniversary.

Author contributions P.D., Y.D., J.C.K. and H.W. conceived the study and designed experiments. P.D. and W.M. designed and cloned constructs. P.D. and W.M. performed preliminary expression and purification studies. P.D. purified proteins and performed biochemical assays. P.D. performed cell-based experiments. P.D. purified the caspase-4–pro-IL-18 complex for structural studies. Y.D. and P.D. generated cryo-EM grids for data collection. Y.D. screened cryo-EM grids and collected cryo-EM data. Y.D. analysed cryo-EM data and performed model building and refinement. J.M. performed cross-linking MS and data analysis under the supervision of S.P.G. P.D., Y.D., J.C.K. and H.W. wrote the manuscript with input from all of the other authors.

Competing interests J.C.K. consults and holds equity in Corner Therapeutics, Larkspur Biosciences and Neumora Therapeutics. H.W. is a co-founder and chair of the scientific advisory board of Ventus Therapeutics. None of these relationships influenced this study. The other authors declare no competing interests.

Additional information

Supplementary information The online version contains supplementary material available at https://doi.org/10.1038/s41586-023-06751-9.

Correspondence and requests for materials should be addressed to Hao Wu or Jonathan C. Kagan.

Peer review information *Nature* thanks Osamu Nureki and the other, anonymous, reviewer(s) for their contribution to the peer review of this work.

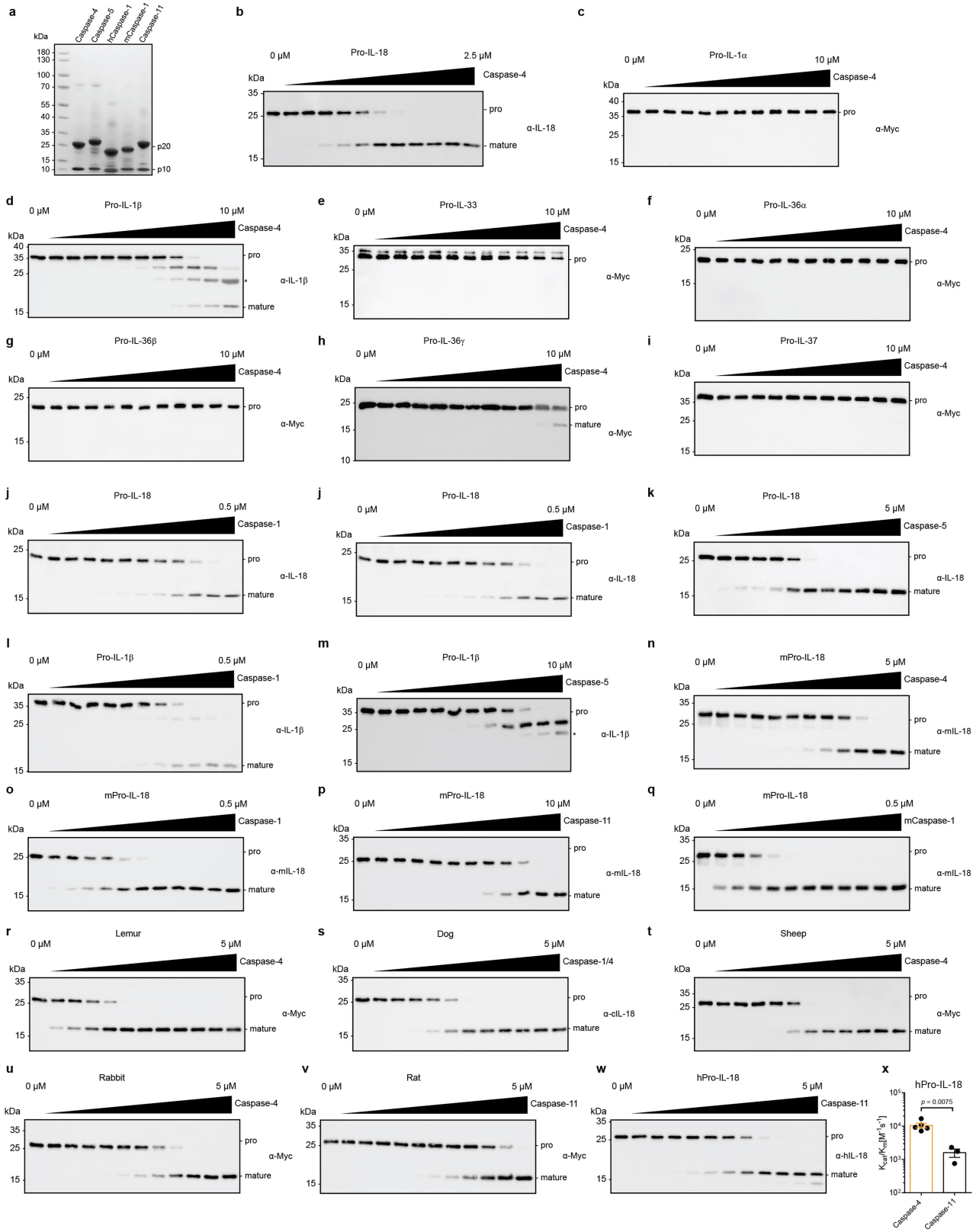

Extended Data Fig. 1 | See next page for caption.

Extended Data Fig. 1 | Comparative analysis of IL-1 cytokine cleavage across mammals. a, 10 μg of indicated proteins were separated by SDS-PAGE and stained with InstantBlue. **b**-**k**, In vitro cleavage of pro-forms of indicated human IL-1 family cytokines by caspase-4, caspase-1 and caspase-5. Immunoblots are representative of three independent repeats. Asterisk marks signal due to cross-reaction of primary antibody with His-tagged p20 subunit of the caspase. **l**,**m**, Immunoblots showing in vitro cleavage of human pro-IL-1β by human caspase-1 and caspase-5. Asterisk marks signal due to cross-reaction of primary antibody with His-tagged p20 subunit of the caspase. **n**-**q**, Immunoblots showing in vitro cleavage of murine pro-IL-18 by human caspase-1 and caspase-4, and murine caspase-1 and caspase-11. **r**–**v**, Immunoblots showing in vitro cleavage of pro-IL-18 from indicated mammalian species by caspase-4 homologue from the same species. **w**, **x**, Immunoblot and quantification of in vitro cleavage of human pro-IL-18 mutants by murine caspase-11. n = 4 biological replicates for caspase-4 and n = 3 biological replicates for caspase-11. All immunoblots are representative of at least three biological replicates. Bars and error bars represent mean ± SEM. Statistical significance was determined by unpaired, two-sided student's t-test. For gel source data, see Supplementary Fig. 1.

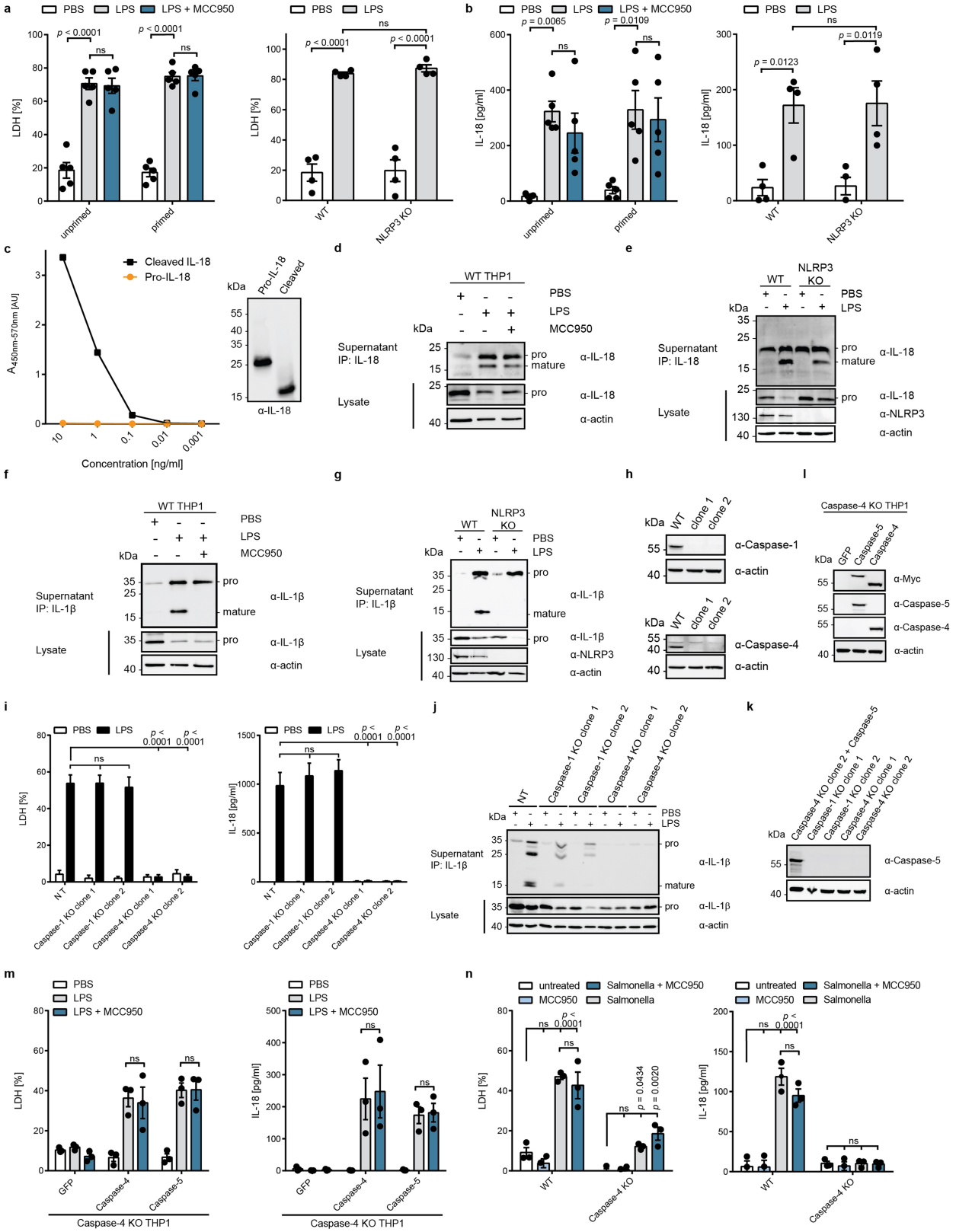

Extended Data Fig. 2 | See next page for caption.

Extended Data Fig. 2 | Cytosolic LPS induces NLRP3-independent IL-18 release from human cells. a, **b**, WT or NLRP3-deficient THP1 monocytes were primed with Pam3CSK4, or left unprimed, and electroporated with LPS (or PBS) in presence or absence of MCC950 and LDH and IL-18 release into supernatant was quantified after 2 h. **c**, ELISA analysis of purified pro-IL-18 and mature IL-18. Mature IL-18 was generated by cleavage of pro-IL-18 with recombinant caspase and complete cleavage was confirmed by immunoblot. Immunoblot and ELISA results are representative of two experiments. **d**, **e**, WT or NLRP3-deficient THP1 monocytes were electroporated with LPS (or PBS) in the presence of absence of MCC950. IL-18 from cell culture supernatants was immunoprecipitated and analysed by immunoblot. **f**, **g**, Pam3CSK4-primed WT or NLRP3-deficient THP1 monocytes were electroporated with LPS (or PBS) in the presence of absence of MCC950. IL-1β was immunoprecipitated from supernatants and analysed by immunoblot. **h**, Immunoblot analysis of THP1 cells in which expression of caspase-1 or caspase-4 was disrupted by CRISPR–Cas9. **i**, **j**, LPS-primed THP1 macrophages deficient for caspase-1, caspase-4 or treated with a non-target sgRNA (NT) were electroporated with LPS (or PBS) and LDH release and IL-18 levels in supernatants were quantified after 2 h. IL-1β from supernatants was immunoprecipitated and analysed by immunoblot. Immunoblot is representative of three biological replicates. **k**, Immunoblot analysis of LPS-primed caspase-1 or caspase-4-deficient THP1 macrophages compared to caspase-4-deficient THP1 cells reconstituted with caspase-5 by retroviral transduction. Cells were differentiated into macrophages and stimulated with LPS for 4 h. **l**, Immunoblot analysis of caspase-4-deficient THP1 cells reconstituted with caspase-4 or caspase-5 by retroviral transduction. **m**, Caspase-4-deficient THP1 macrophages expressing GFP only, caspase-4 or caspase-5 were primed with LPS before delivery of LPS into the cytosol by electroporation. LDH and IL-18 release into supernatants was quantified after 2 h. **n**, WT or caspase-4-deficient THP1 macrophages were infected with a flagellin-deficient strain of Salmonella and LDH and IL-18 release was quantified after 24 h. Immunoblots are representative of three (**d**, **e**, **f**, **g**, **h**, **j**) or two (**h**, **l**, **k**, **c**) biological replicates. Bars and error bars represent mean ± SEM of three (**i, n**), four (**a, b** right panels) or five (**a, b** left panel) biological replicates. Statistical significance was determined by two-way ANOVA with Tukey's multiple comparisons test: ns = not significant ($p > 0.05$). For gel source data, see Supplementary Fig. 1.

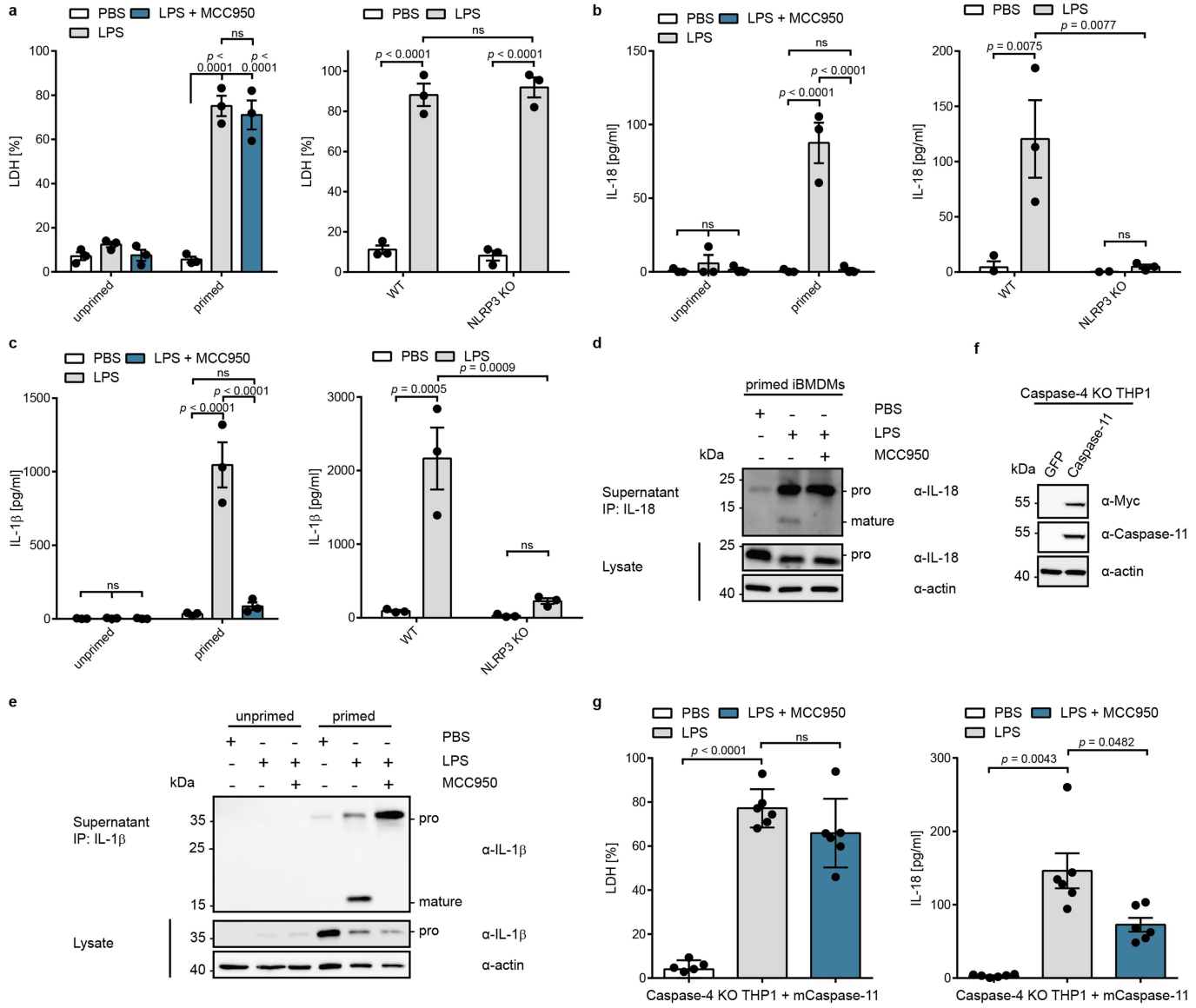

Extended Data Fig. 3 | Cytosolic LPS-induced IL-18 release from murine cells is NLRP3-dependent. a, **b**, **c**, WT or NLRP3-deficient iBMDMs were primed with extracellular LPS, or left unprimed, and electroporated with LPS (or PBS) in the presence of absence of MCC950. LDH, IL-18 and IL-1β release into supernatant was quantified after 2 h. n = 3 biological replicates. **d**, **e**, LPS-primed WT iBMDMs were electroporated with LPS (or PBS) in the presence or absence of MCC950. IL-18 and IL-1β were immunoprecipitated from supernatants and analysed by immunoblot (representative of three biological replicates). **f**, Immunoblot analysis caspase-4-deficient THP1 cells reconstituted with caspase-11 by retroviral transduction (representative of two independent repeats). **g**, Caspase-4-deficient THP1 macrophages expressing caspase-11 were primed with extracellular LPS, or left unprimed, and electroporated with LPS (or PBS) in the presence of absence of MCC950. LDH, and IL-18 release into supernatant was quantified. n = 6 biological replicates. Bars and error bars represent mean ± SEM. Statistical significance was determined by two-way ANOVA (a,b,c) or one-way ANOVA (g) with Tukey's multiple comparisons test: ns = not significant ($p > 0.05$). For gel source data, see Supplementary Fig. 1.

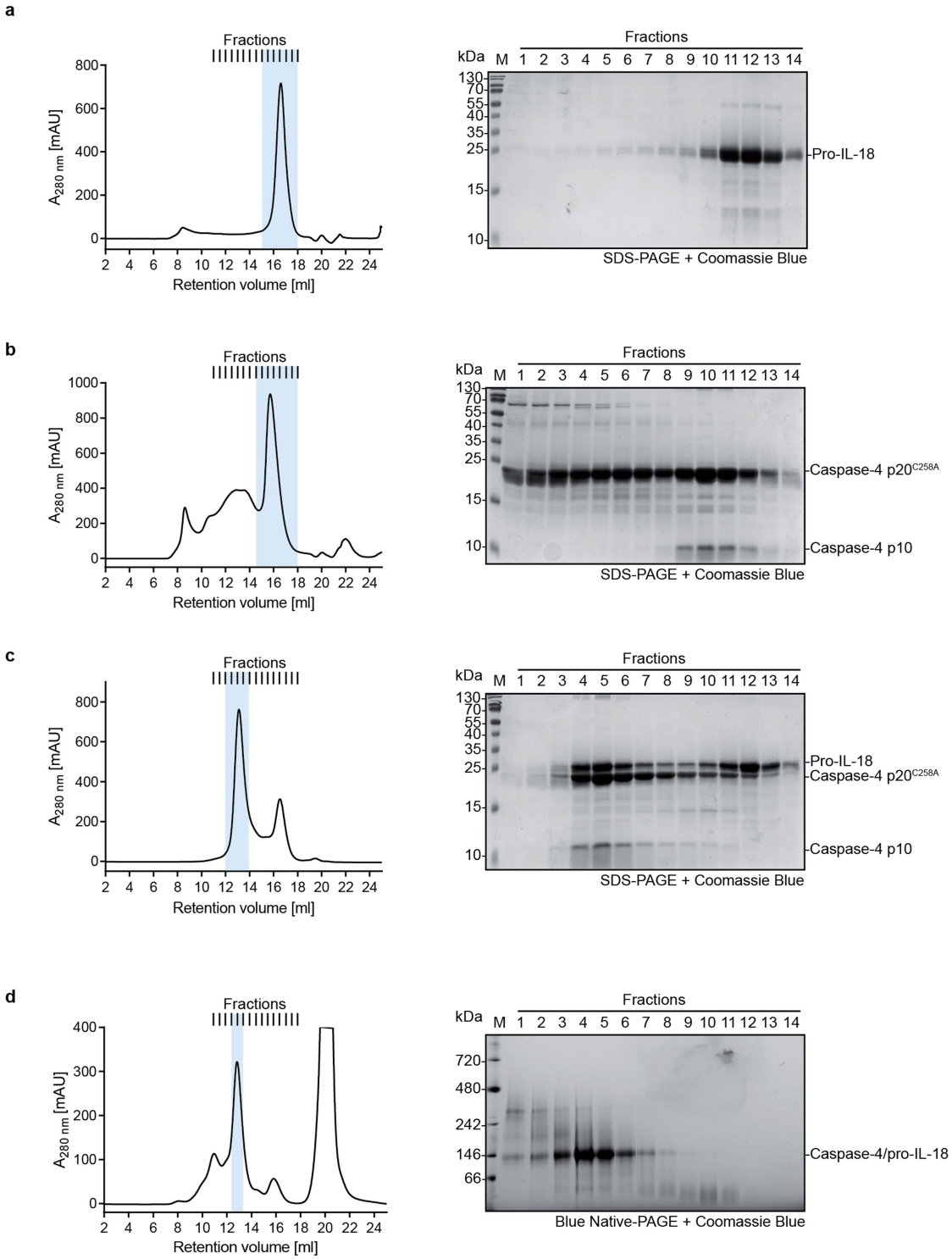

Extended Data Fig. 4 | Assembly and purification of a recombinant caspase-4/pro-IL-18 complex. a, SEC profile and corresponding coomassie-stained SDS-PAGE gel of purified pro-IL-18 expressed in insect cells. **b**, SEC profile and corresponding coomassie-stained SDS-PAGE gel of purified catalytically inactive caspase-4 p20/p10 expressed in *E. coli*. **c**, SEC profile and corresponding coomassie-stained SDS-PAGE gel of a complex consisting of caspase-4 p20/p10 and pro-IL-18. Complex was assembled by co-incubation at 37 °C for 20 min. **d**, SEC profile and corresponding coomassie-stained Blue Native-PAGE gel of a complex consisting of caspase-4 p20/p10 and pro-IL-18 crosslinked with BS3. Gels and SEC profiles are representative of at least two independent purifications. Peak fractions that were combined for downstream applications are highlighted in blue. For gel source data, see Supplementary Fig. 1.

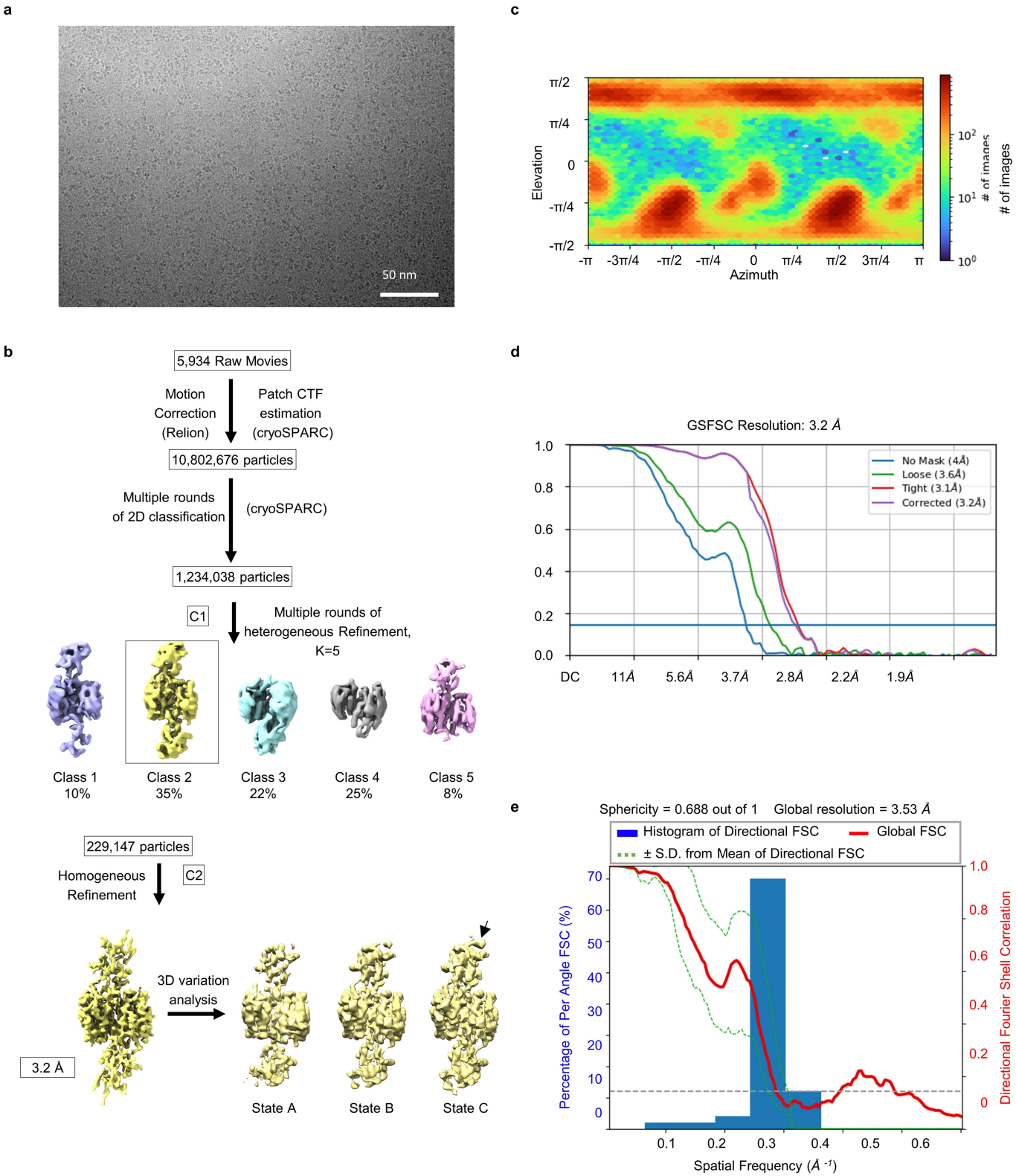

Extended Data Fig. 5 | Cryo-EM data processing for the caspase-4/pro-IL-18 complex. a, Cryo-EM raw image (representative of two data collections). **b**, Cryo-EM data processing flow chart. The black arrow pointing to "State C" shows domain flexibility indicated by 3D variability analysis. **c**, Heat map for the orientation of particles used for the final reconstruction. **d**, Fourier shell correlation (FSC) plots. **e**, 3D FSC plot.

a

Crosslinking between caspase-4 and pro-IL-18

Caspase-4	Pro-IL-18	Cα-Cα (Å)
287-GASAVYKT-294	94-RGMAVTISVKCEKI-107	22.3
287-GASAVYKT-294	140-RSVPGHDNKMQFES SSYEGYFLACEKE-166	17.4
354-RAKAQMPTIERL-365	17-KFIDNTLYFIAEDDENL ESDYFGKLESKL-45	18.7
354-RAKAQMPTIERL-365	40-KLESKLSVIRN-50	18.8
354-RAKAQMPTIERL-365	148-KMQFESSSYEGYFLA CEKERD-168	20.8

b

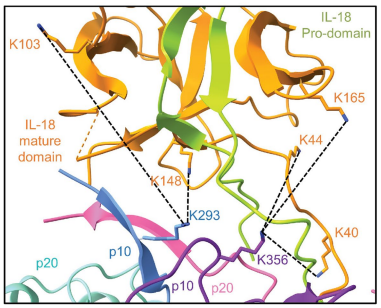

c

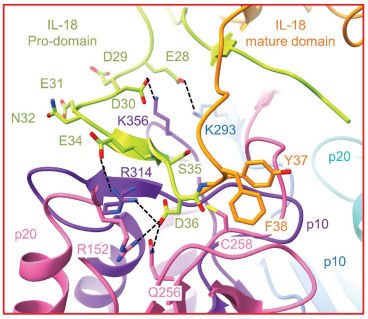

d

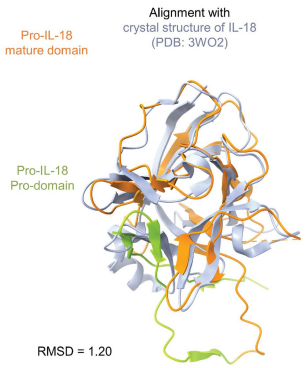

e

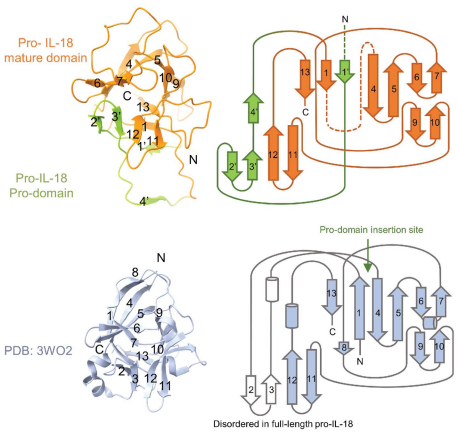

f

Intramolecular crosslinks of pro-IL-18 in caspase-4/pro-IL-18 complex

Pro-IL-18	Pro-IL-18	Cα-Cα (Å) in complex / IL-18
40-KLESKLSVIRN-50	148-KMQFESSSYEGYFLA CEKERD-168	12.6 / 33.6 Too far in IL-18
40-KLESKLSVIRN-50	171-KLILKKE-177	17.4 / 31.9 Too far in IL-18

Intramolecular crosslinks of free pro-IL-18

Pro-IL-18	Pro-IL-18	Cα-Cα (Å) in complex / IL-18
40-KLESKLSVIRN-50	120-KEMNPPDNIKDTKS-133	35.9 / 28.6 Not consistent with either
40-KLESKLSVIRN-50	148-KMQFESSSYEGYFLA CEKERD-168	12.6 / 33.6 Too far in IL-18

All the remaining pairs are consistent with structures of both the caspase-4/pro-IL-18 complex and mature IL-18.

g

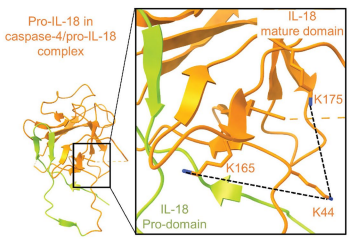

h

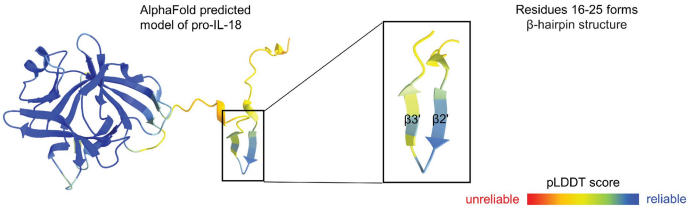

Extended Data Fig. 6 | Crosslinking mass spectrometry analysis of caspase-4/pro-IL-18 complex and structural comparison between caspase-4-bound pro-IL-18 and free IL-18. a, Summary of BS3 crosslinking between caspase-4 and pro-IL-18. The crosslinked peptides with high confidence are shown with residue ranges, and colour labelled by their domain colour except for the crosslinked Lys residues which are in red. **b**, Crosslinked lysine pairs between caspase-4 and pro-IL-18 mapped onto the structure of the caspase-4/pro-IL-18 complex and indicated by black dash lines. **c**, The molecular interaction of the active form of caspase-4 interacting with pro-IL-18. Model was derived by replacing Ala258 with Cys. **d**, **e**, Structural alignment between pro-IL-18 bound to caspase-4 and the crystal structure of mature IL-18 (d) and in topology diagrams (e). β-strands are labelled sequentially with those in the pro-domain denoted by a prime (′). **f**, Crosslinked lysine pairs within pro-IL-18 in the caspase-4/pro-IL-18 complex (upper table), and those within pro-IL-18 alone before incubating with caspase-4 (lower table). The former pairs are consistent with the caspase-4/pro-IL-18 complex structure, but not the mature IL-18 structure, and the latter pairs are not consistent with any IL-18 structures, suggesting that the pro-IL-18 conformation may be different before caspase-4 binding. **g**, Crosslinked lysine pairs within pro-IL-18 mapped onto the structure of the caspase-4/pro-IL-18 complex and indicated by black dash lines. **h**, AlphaFold predicted model of pro-IL-18 coloured by per-residue pLDDT score, ranging from unreliable in red to reliable in blue. Residues 16-25 of the pro-domain form a β-hairpin structure, consistent with our cryo-EM structure pro-IL-18 in complex with caspase-4.

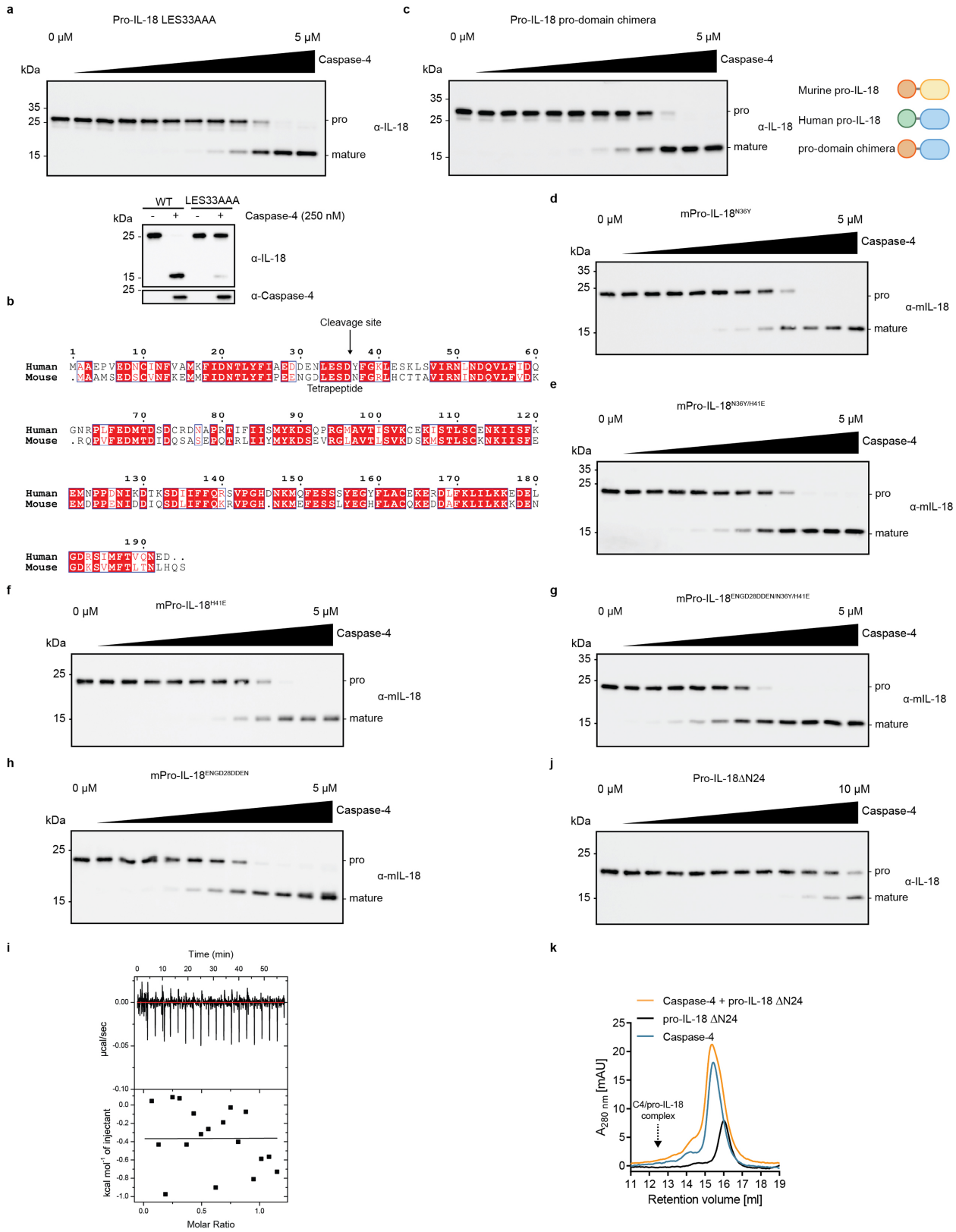

Extended Data Fig. 7 | The pro-domain of pro-IL-18 mediates the interaction with caspase-4. a, **c**, Immunoblots showing in vitro cleavage of pro-IL-18 mutants by caspase-4. The pro-domain chimera consists of the pro-domain of murine pro-IL-18 fused to the mature domain of human pro-IL-18. Immunoblots are representative of three biological replicates. **b**, Sequence alignment of human and murine pro-IL-18. Identical and similar amino acids are highlighted in red or white boxes, respectively. Sequences were aligned using ClustalOmega online tool and plotted in ESPript 3.0. **d**-**h**, Immunoblots showing in vitro cleavage of murine pro-IL-18 mutants by caspase-4. **i**, ITC analysis of binding of mature IL-18 to WT caspase-4. **j**, Immunoblots showing in vitro cleavage of human pro-IL-18 ΔN24 by caspase-4. Pro-IL-18 ΔN24 lacks the first 24 amino acids at the N-terminus. **k**, Analytical SEC demonstrating no binding between pro-IL-18 ΔN24 and caspase-4. All data are representative of three independent repeats. For gel source data, see Supplementary Fig. 1.

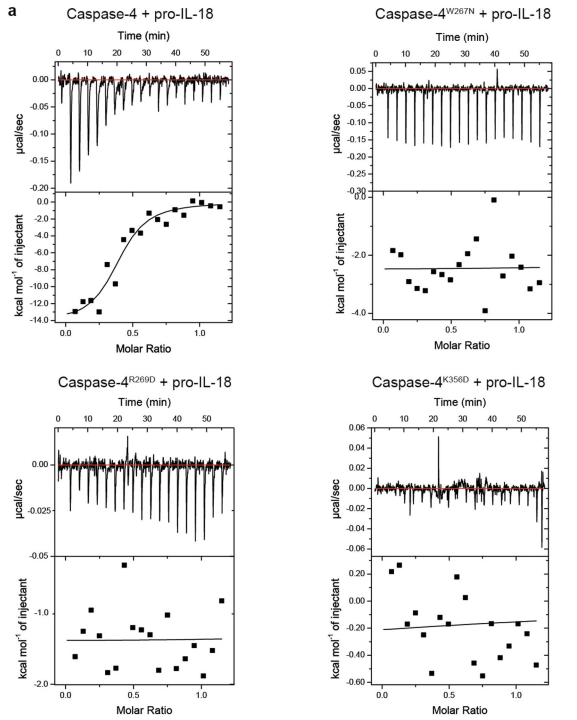

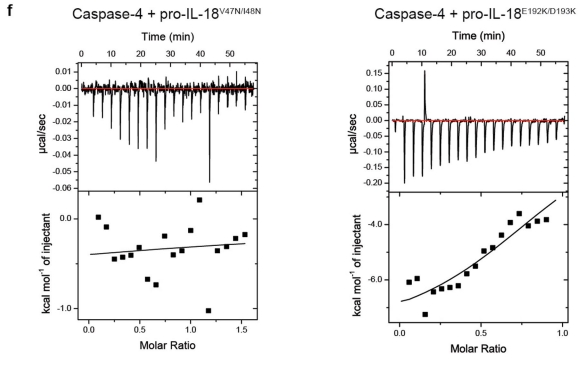

g

Caspase-4 +	K_D [µM]	Stoichiometry factor
Pro-IL-18$^{E192K/D193K}$	8.9 ± 1.5	1.32 ± 0.40
pro-IL-18$^{V47N/I48N}$	n.d	n.d.

b

Pro-IL-18 +	K_D [µM]	Stoichiometry factor
Caspase-4	1.2 ± 0.3	0.56 ± 0.17
Caspase-4^{W267N}	n.d	n.d.
Caspase-4^{R269D}	n.d	n.d.
Caspase-4^{K356D}	n.d	n.d.

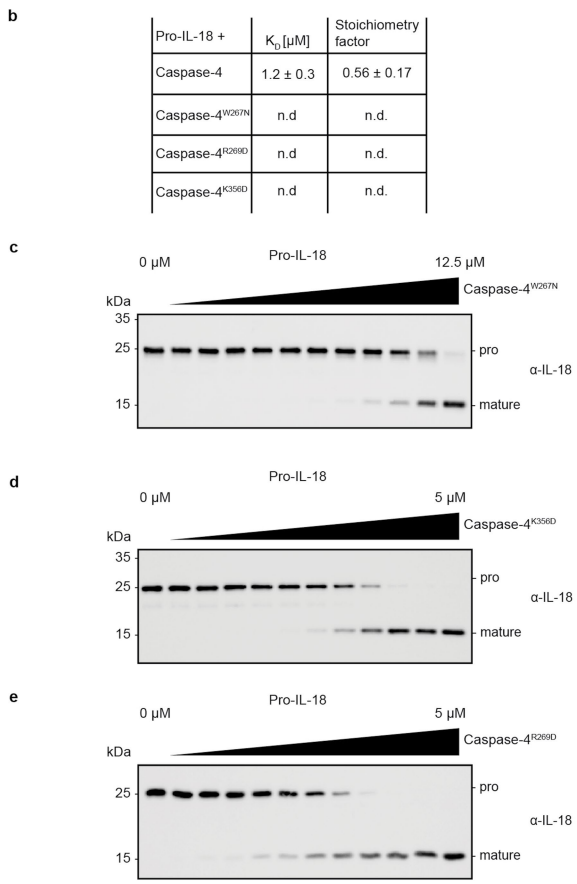

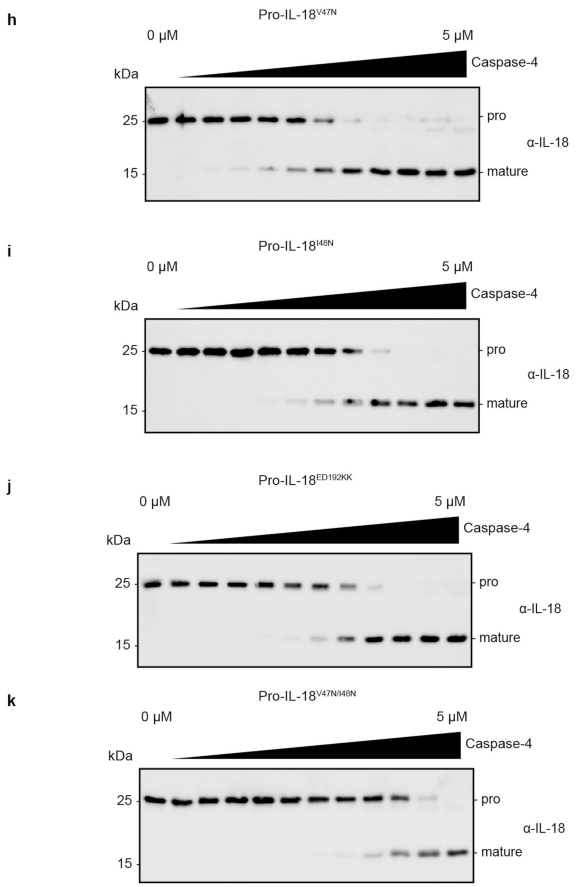

Extended Data Fig. 8 | Biochemical characterization of caspase-4 and pro-IL-18 mutants that disrupt interaction interfaces with pro-IL-18. **a**, ITC analysis of binding of pro-IL-18 (purified from insect cells) to caspase-4 mutants. **b**, Thermodynamic parameters of binding of indicated caspase-4 mutants to pro-IL-18 as determined by ITC. **c**, **d**, **e**, Immunoblots showing in vitro cleavage of human pro-IL-18 by indicated caspase-4 mutants. **f**, ITC analysis of binding of indicated pro-IL-18 mutants (purified from *E. coli*) to WT caspase-4. Graphs are representative of at least three biological replicates. **g**, Thermodynamic parameters of binding of caspase-4 mutants to pro-IL-18 as determined by ITC. **h**-**k**, Immunoblots showing in vitro cleavage of indicated human pro-IL-18 variants by caspase-4. Immunoblots are representative of three biological replicates. ITC graphs are representative of three independent repeats. ITC results represent mean ± SD of three independent measurements. n.d. = no binding detected. For gel source data, see Supplementary Fig. 1.

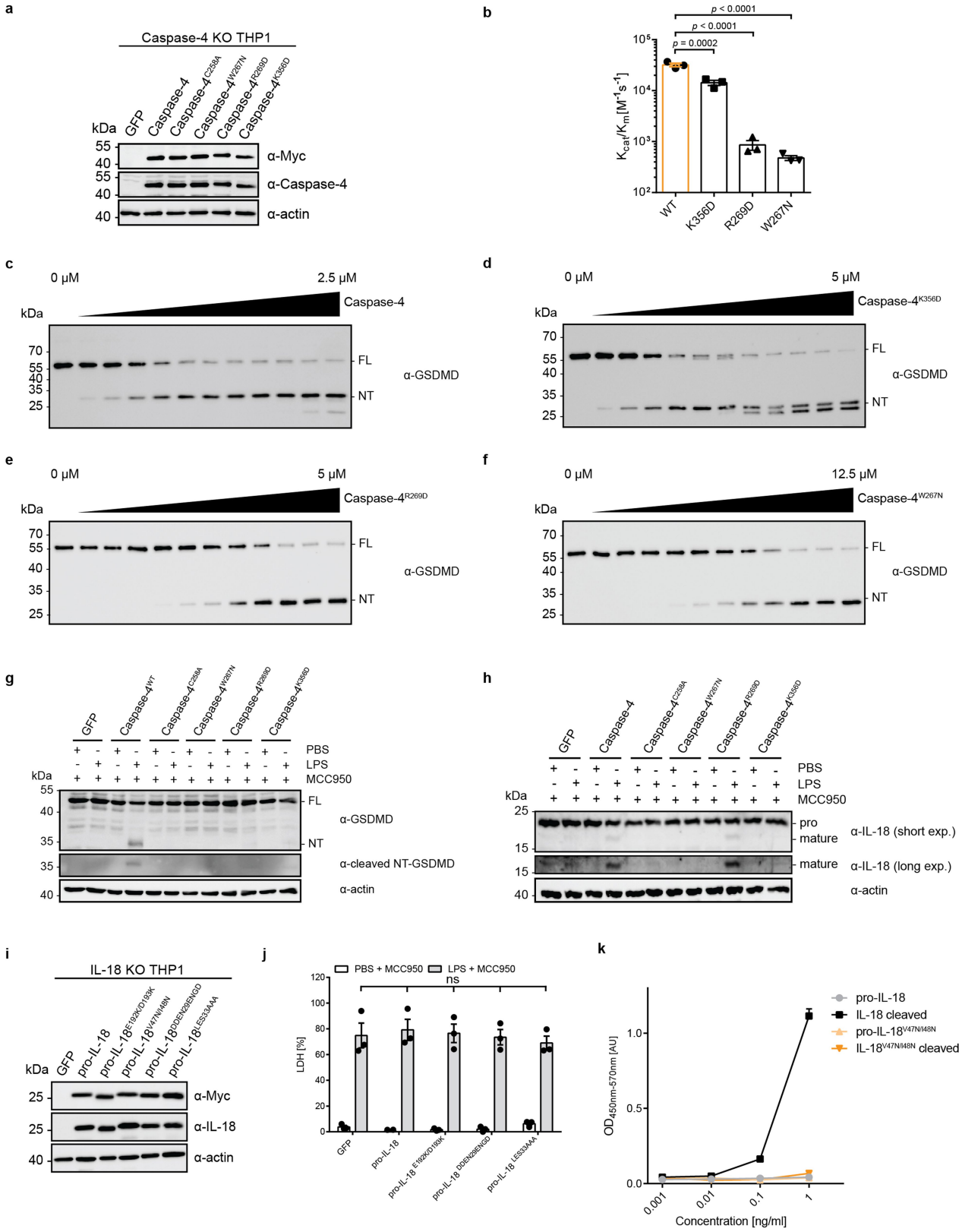

Extended Data Fig. 9 | See next page for caption.

Extended Data Fig. 9 | Effect of structure-based mutations in caspase-4 on GSDMD and pro-IL-18 cleavage in cells. a, Expression of indicated caspase-4 mutants in caspase-4-deficient THP1 cells (representative of two independent repeats). **b**, In vitro cleavage of human GSDMD by caspase-4 mutants. **c**–**f**, Immunoblots showing in vitro cleavage of pro-IL-18 by caspase-4 mutants. Immunoblots are representative of three independent repeats. **g**, **h**, Caspase-4-deficient THP1 macrophages expressing caspase-4 mutants were primed with LPS and electroporated with LPS (or PBS). Processing of GSDMD and pro-IL-18 was analysed by immunoblot. Immunoblots are representative of three biological replicates. **i**, Immunoblot showing expression of indicated pro-IL-18 mutants in IL-18-deficient THP1 cells (representative of two independent repeats). **j**, IL-18-deficient THP1 cells expressing pro-IL-18 mutants were electroporated with LPS (or PBS) in the presence of MCC950 and release of LDH into cell culture supernatant was quantified after 2 h. **k**, ELISA analysis demonstrating that pro-IL-18$^{V47N/I48N}$ is not recognized by the used ELISA reagent. ELISA results are displayed as mean ± SD of two technical replicates and are representative of two independent biological replicates. Bars and error bars in **b**, **j** represent mean ± SEM of three biological replicates. Each data point represents result of one independent experiment. Statistical significance was determined by two-way ANOVA with Tukey's multiple comparisons test: ns = not significant ($p > 0.05$). For gel source data, see Supplementary Fig. 1.

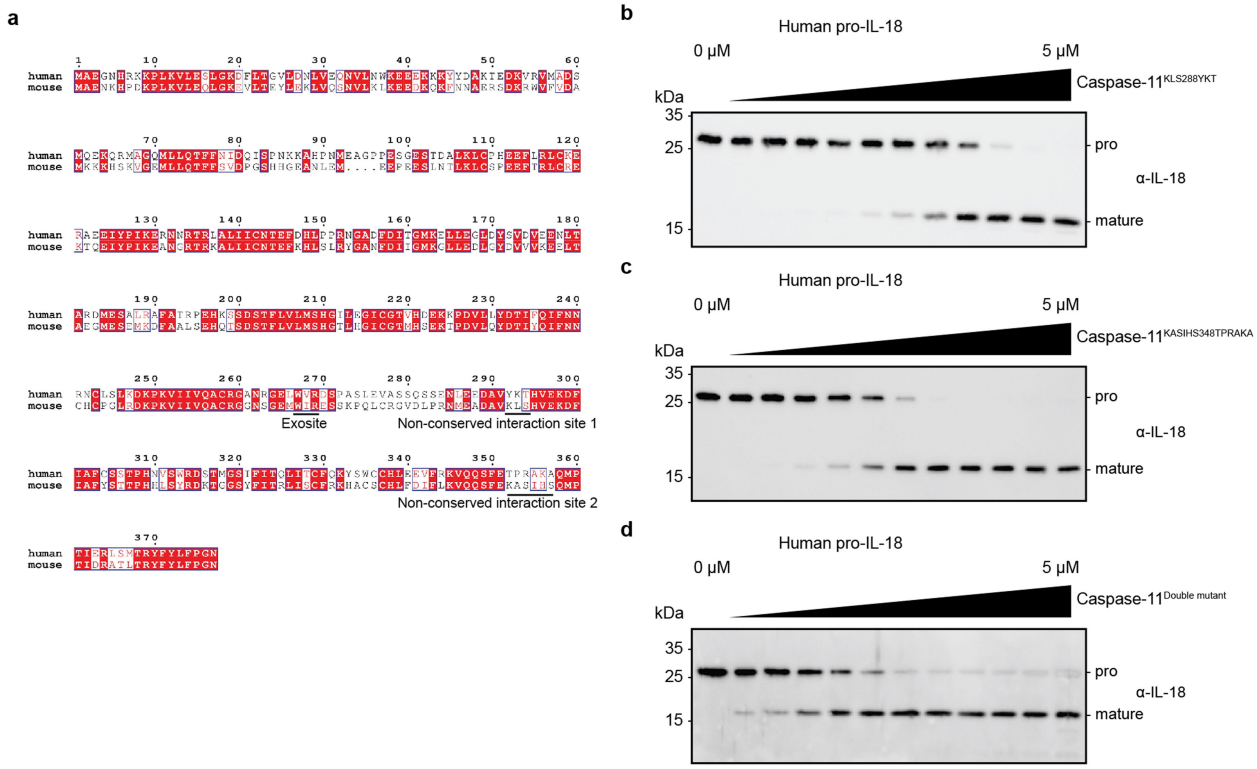

Extended Data Fig. 10 | Mutagenesis of murine caspase-11 based on structural and sequence alignments. a, Sequence alignment of human caspase-4 and murine caspase-11. Identical and similar amino acids are highlighted in red or white boxes, respectively. Sequences were aligned using ClustalOmega and plotted in ESPript 3.0. **b**, **c**, **d**, Immunoblots showing in vitro cleavage of human pro-IL-18 by caspase-11 mutants. Immunoblots are representative of three biological replicates. For gel source data, see Supplementary Fig. 1.

Extended Data Table 1 | Data collection, data processing and validation statistics

Data Collection and Processing	
Microscope	Titan Krios
Voltage (keV)	300
Camera	K3
Magnification	105,000
Pixel size at detector (Å/pixel)	0.83
Total electron exposure ($e^-/Å^2$)	60.8
Exposure rate (e^-/pixel/sec)	28.6
Number of frames collected during exposure	50
Defocus range (μm)	-1.0 to -2.5
Automation software	SerialEM 3.8
Energy filter slit width (eV)	20
Micrographs collected (no.)	5,934
Micrographs used (no.)	5,732
Total extracted particles (no.)	10,802,676
Refinement	
Refined particles (no.) / Final particles (no.)	1,234,038/229,147
Symmetry parameters	C2
Map resolution (Å)	3.2
FSC 0.143 (unmasked / masked)	4.0/3.2
Resolution range (Å)	2.9 to 11.1
Resolution range due to anisotropy (Å)	3.3 to 3.7
Map sharpening *B* factor range ($Å^2$)	-144.2
Map sharpening methods	LocalDeblur
Model composition	
Chains	6
Protein residues	828
Validation	
Model-Map scores	
CC (correlation coefficients)	0.78
Average FSC (0 / 0.143 / 0.5)	2.5/3.3/3.5
R.m.s. deviations from ideal values	
Bond lengths (Å)	0.003
Bond angles (°)	0.731
MolProbity score	2.04
CaBLAM outliers	3.52
Clashscore	10.41
Poor rotamers (%)	1.18
C-beta outliers (%)	0.00
Ramachandran plot	
Favoured (%)	93.1
Allowed (%)	6.9
Outliers (%)	0.00

nature portfolio

Corresponding author(s): Jonathan C. Kagan, Hao Wu

Last updated by author(s): 09-29-2023

Reporting Summary

Nature Portfolio wishes to improve the reproducibility of the work that we publish. This form provides structure for consistency and transparency in reporting. For further information on Nature Portfolio policies, see our Editorial Policies and the Editorial Policy Checklist.

Statistics

For all statistical analyses, confirm that the following items are present in the figure legend, table legend, main text, or Methods section.

n/a	Confirmed
☐	☒ The exact sample size (*n*) for each experimental group/condition, given as a discrete number and unit of measurement
☐	☒ A statement on whether measurements were taken from distinct samples or whether the same sample was measured repeatedly
☐	☒ The statistical test(s) used AND whether they are one- or two-sided *Only common tests should be described solely by name; describe more complex techniques in the Methods section.*
☐	☒ A description of all covariates tested
☐	☒ A description of any assumptions or corrections, such as tests of normality and adjustment for multiple comparisons
☐	☒ A full description of the statistical parameters including central tendency (e.g. means) or other basic estimates (e.g. regression coefficient) AND variation (e.g. standard deviation) or associated estimates of uncertainty (e.g. confidence intervals)
☐	☒ For null hypothesis testing, the test statistic (e.g. *F*, *t*, *r*) with confidence intervals, effect sizes, degrees of freedom and *P* value noted *Give P values as exact values whenever suitable.*
☒	☐ For Bayesian analysis, information on the choice of priors and Markov chain Monte Carlo settings
☒	☐ For hierarchical and complex designs, identification of the appropriate level for tests and full reporting of outcomes
☒	☐ Estimates of effect sizes (e.g. Cohen's *d*, Pearson's *r*), indicating how they were calculated

Our web collection on statistics for biologists contains articles on many of the points above.

Software and code

Policy information about availability of computer code

Data collection	Cryo-EM data collection: SerialEM (version 3.8).
Data analysis	Cryo-EM data analysis: MotionCor2 (version 1.1.0), Relion (version 3.08), Coot (version 0.8.9), PHENIX (version 1.17.1). Sequence alignment: Clustal v. Omega (accessed through the EMBL-EBI server); ESPript 3.0 Molecular Graphics: UCSF ChimeraX (version 1.4) and PyMOL (version 2.5.2). Immunoblot quantification: ImageJ (version 1.51). Data plotting: GraphPad Prism v.6.01, Origin v.7.0 Protein structure prediction: Alphafold 2.0

For manuscripts utilizing custom algorithms or software that are central to the research but not yet described in published literature, software must be made available to editors and reviewers. We strongly encourage code deposition in a community repository (e.g. GitHub). See the Nature Portfolio guidelines for submitting code & software for further information.

Data

Policy information about availability of data

All manuscripts must include a data availability statement. This statement should provide the following information, where applicable:

- Accession codes, unique identifiers, or web links for publicly available datasets
- A description of any restrictions on data availability
- For clinical datasets or third party data, please ensure that the statement adheres to our policy

All data and materials reported in the main and supplementary data are available upon request. Raw data needed to recreate plots and uncropped gel images are accessible in the supplementary material of this paper. The electron density maps of caspase-4/pro-IL-18 at 3.2 Å have been deposited in the Electron Microscopy Data Bank (EMDB) with accession codes EMD-40678. The atomic coordinates for caspase-4/pro-IL-18 have been deposited in the Protein Data Bank with the accession code of 8SPB. Atomic coordinates for mature IL-18 and caspase-11 were downloaded from the Protein Data Bank under the accession codes 3WO2 and 6KN1, respectively.

Research involving human participants, their data, or biological material

Policy information about studies with human participants or human data. See also policy information about sex, gender (identity/presentation), and sexual orientation and race, ethnicity and racism.

Reporting on sex and gender	Human blood samples were derived from anonymous donors without reporting on sex and gender.
Reporting on race, ethnicity, or other socially relevant groupings	Human blood samples were derived from anonymous donors without reporting on race, ethnicity.
Population characteristics	*Describe the covariate-relevant population characteristics of the human research participants (e.g. age, genotypic information, past and current diagnosis and treatment categories). If you filled out the behavioural & social sciences study design questions and have nothing to add here, write "See above."*
Recruitment	*Describe how participants were recruited. Outline any potential self-selection bias or other biases that may be present and how these are likely to impact results.*
Ethics oversight	*Identify the organization(s) that approved the study protocol.*

Note that full information on the approval of the study protocol must also be provided in the manuscript.

Field-specific reporting

Please select the one below that is the best fit for your research. If you are not sure, read the appropriate sections before making your selection.

☒ Life sciences ☐ Behavioural & social sciences ☐ Ecological, evolutionary & environmental sciences

For a reference copy of the document with all sections, see nature.com/documents/nr-reporting-summary-flat.pdf

Life sciences study design

All studies must disclose on these points even when the disclosure is negative.

Sample size	Sample sizes were not pre-determined. Cryo-EM images were collected until structures of satisfactory quality were solved, which suggested sufficient sample size. For biochemical and cellular experiments, no information was derived about a population based on sampling, and therefore sample size determination was not necessary. All biochemical and cell-based experiments were performed at least three times, as is standard in the field.
Data exclusions	In cryo-EM processing, we discarded "junk" particles that could not be classified into useful 3D reconstructions. This is a widely used and accepted practice in the cryo-EM field. No other data were excluded from analysis.
Replication	All experiments were performed independently at least two or three times with similar results, as described in the figure legends.
Randomization	No randomization was performed, as this does not apply to the biochemical and cell-based experiments decribed in this study.
Blinding	Blinding was not performed as subjective analysis was not needed. Each experiment was analyzed using consistent methods. Random allocation and quantitative measurements using various approaches and reaction kits as described in the methods minimized biased assessments.

Reporting for specific materials, systems and methods

We require information from authors about some types of materials, experimental systems and methods used in many studies. Here, indicate whether each material, system or method listed is relevant to your study. If you are not sure if a list item applies to your research, read the appropriate section before selecting a response.

Materials & experimental systems

n/a	Involved in the study
☐	☒ Antibodies
☐	☒ Eukaryotic cell lines
☒	☐ Palaeontology and archaeology
☒	☐ Animals and other organisms
☒	☐ Clinical data
☒	☐ Dual use research of concern
☒	☐ Plants

Methods

n/a	Involved in the study
☒	☐ ChIP-seq
☒	☐ Flow cytometry
☒	☐ MRI-based neuroimaging

Antibodies

Antibodies used

Primary antibodies:
monoclonal rabbit anti-human caspase-1 (Clone D7F10), Cell Signaling, 3866S
polyclonal rabbit anti-human caspase-4, Cell Signaling, 4450S
monoclonal rabbit anti-human caspase-5 (Clone D3G4W), Cell Signaling 46680
monoclonal rabbit anti-Myc tag (Clone 71D10), Cell Signaling, 2278S
monoclonal mouse anti-Myc-tag (Clone 9B11), Cell Signaling, 2276S
monoclonal rabbit anti-murine IL-18 (Clone E8P5O), Cell Signaling, 57058
monoclonal rabbit anti-human GSDMD (Clone E8G3F), Cell Signaling, 97558S
monoclonal mouse-anti caspase-4 (Clone 4B9), Enzo Biosciences, ADI-AAM-114-E
monoclonal mouse anti-mouse and human NLRP3 (Clone Cryo-2), Adipogen, AG-20B-0014-C100
polyclonal rabbit anti-human IL-18, MBL, PM014
monoclonal rabbit anti-cleaved human GSDMD-NT (Clone EPR20829-408), Abcam, (ab215203)
monoclonal rabbit-anti murine IL-18 (Clone EPR19956), Abcam, ab207323
monoclonal rat anti-actin (Clone Poly6221), Biolegend, 622102
monoclonal rat-anti caspase-11 (Clone Cas11.17D9), Biolegend, 647202
monoclonal mouse anti-canine IL-18 (Clone 314820), R&D Systems, MAB2924-SP
polyclonal rabbit anti-human IL-1β, Genetex, GTX130021
polyclonal rabbit anti-murine IL-1β, Genetex, GTX74034
monoclonal mouse-anti actin (Clone AC-15), SigmaAldrich, A5441
polyclonal biotinylated goat anti-murine IL-1β, R&D Systems, BAF401
polyclonal biotinylated goat anti-Human IL-1β, R&D Systems, BAF201
Secondary antibodies:
HRP-Goat Anti-Rabbit IgG (H+L), Jackson ImmunoResearch, 111-035003
HRP-Goat Anti-Rat IgG (H+L), Jackson ImmunoResearch, 112-035-167
HRP-Goat Anti-Mouse IgG (H+L), Jackson ImmunoResearch, 115-035-003

Validation

Antibodies against human caspase-1, caspase-4 and IL-18 were validated in this study by immunoblot on THP1 cells deficient for these genes generated by CRISPR/Cas9 (See immunoblots in Extended Data Figures 3h and 11i) . All other antibodies used in this study have been validated by the manufacturers and in peer-reviewed publications as detailed on the manufacturer's website.

Eukaryotic cell lines

Policy information about cell lines and Sex and Gender in Research

Cell line source(s)

WT THP1 cells from ATCC, NLRP3KO THP1 cells from Invivogen, Sf9 insect cells from ThermoFisher, immortalized bone marrow-derived macrophages were generated in the Jonathan Kagan Laboratory from the bone-marrow of female WT C57BL/6J or NLRP3 KO mice (B6.129S6-Nlrp3tm1Bhk/J).

Authentication

Cell lines were verified by manufacturer's website and identity were checked by their morphological features

Mycoplasma contamination

THP1 cells tested negative for mycoplasma contamination using MycoStrip kit (Invivogen). Other cell lines were not frequently tested.

Commonly misidentified lines
(See ICLAC register)

No commonly misidentified cell lines were used in this study.